Universidade de Aveiro Departamento de Engenharia Cerâmica e do Vidro
2009

Mengistie Leweyehu Debasu

Síntese e Estudo Fotoluminescencia de Nanofios/Nanobastões de ZnO

Synthesis and Photoluminescence Study of ZnO Nanowires/Nanorods

Universidade de Aveiro Departamento de Engenharia Cerâmica e do Vidro
2009

Mengistie Leweyehu Debasu

Síntese e Estudo Fotoluminescencia de Nanofios/Nanobastões de ZnO

Synthesis and Photoluminescence Study of ZnO Nanowires/Nanorods

Dissertação apresentada à Universidade de Aveiro para cumprimento dos requisitos necessários à obtenção do grau de mestre do Mestrado Europeu em Ciência dos Materiais, realizada sob a orientação científica do Doutor Luís António Ferreira Martins Dias Carlos, Professor catedrático no Departamento de Física da Universidade de Aveiro e Doutora Maria Rute de Amorim e Sá Ferreira André, Investigadora Auxiliar no Laboratório Associado CICECO da Universidade de Aveiro e Professora auxiliares convidada do Departamento de Física da Universidade de Aveiro, e do Doutor Lars Rosgaard Jensen Professor Associado do Departamento de Engenharia Mecânica da Aalborg Universitet.

A dissertation presented to the University of Aveiro in partial fulfilment of the requirements for the awarding of the Joint European Master degree in Materials Science carried out under the supervision of Luís António Ferreira Martins Dias Carlos, Full professor at the Physics Department of University of Aveiro and Maria Rute de Amorim e Sá Ferreira André, Assistant researcher at the Associated Laboratory CICECO at University of Aveiro and Invited Assistant Professor at Physics department of University of Aveiro, and Lars Rosgaard Jensen, Associate Professor at the Mechanical Engineering Department of Aalborg University.

Financial support from European Commission
under the Erasmus Mundus Programme

Dedicated to my father.

O júri

Presidente

Prof. Doutor Vítor Brás Sequeira Amaral
Professor Associado com Agregação da Universidade de Aveiro (Presidente)

Prof. Doutor Luís António Ferreira Martins Dias Carlos
Professor Catedrático da Univesidade de Aveiro (Orientador)

Prof. Doutora Maria Rute de Amorim e Sá Ferreira André
Professora Auxiliar Convidada, Univesidade de Aveiro (Co-orientador)

Prof. Doutor Manfred Niehus
Equiparado a Professor Adjunto do Instituto Superior de Engenharia de Lisboa

Acknowledgment

First, I would like to thank my supervisors, Prof. Luís D. Carlos, Prof. Maria Rute André and Prof. Lars Rosgaard Jensen, for their constructive guidance, comments and encouragement which made me very strong and happy to accomplish this thesis on time and successfully. The lectures given by Prof. Luís D. Carlos and Prof. Lars during my study have helped me a lot for the successfulness of the work. I have been also evaluated by Prof. Luís D. Carlos in writing literature reviews for some courses during the study. I appreciate all the experiences that I have got from these professionals.

I would like to extend my thanks to Thomas Sørensen, Marta Ascensão and Prof. L. B. Augusto for their practical assistance in the SEM images, to Sónia Nobre for her clarification and guidance during the PL measurements, to Rosário Soares for her help in providing me all the XRD data. It is also my great pleasure to thank my friend Fikadu L. for our good teamwork during the synthesis and all the EMMS-4 students with whom I have spent very enjoyable time throughout the whole study period.

I have special thanks to my father who has provided me unreserved and valuable support, courage, and advice to be successful throughout my studies. I would like to express my great respect and appreciation to my mother, brothers and sisters for their wonderful love towards me. I would like also to express my deepest love to my wife Mastewal for her love, moral encouragement and understanding during my stay in this study.

Finally, my gratitude extends to the European Commission for providing me all the financial support to complete the Joint European Master's programme in Materials Science (EMMS). I appreciate all coordinators of the program.

Palavras-chave ZnO, nanoestrutura, evaporação térmica, supersaturação, nanofios, nanobastões, fotoluminescência.

Resumo Os nanofios/nanobastões de ZnO foram sintetizados por evaporação térmica em substratos de alumina (Al_2O_3) e silício (Si). A morfologia, estrutura cristalina e propriedades ópticas dos nanofios/nanobastões foram caracterizadas por microscopia electrónica de varrimento (SEM), difracção de raios-X (XRD), e fotoluminescência em modo de excitação (PLE) e emissão (PL). Através das imagens de SEM é possível concluir que as morfologias dos nanofios/nanobastões dependem de parâmetros de síntese, tais como, temperatura, substrato e velocidade de fluxo de gases de O_2 e N_2. A nucleação e o crescimento dos nanofios/nanobastões são, também, discutidos com base no mecanismo de crescimento vapor-sólido. Os resultados de XRD mostram que os nanofios/nanobastões apresentam a fase wurzite hexagonal do ZnO. O espectro de PL, à temperatura ambiente, mostra duas bandas, nomeadamente, uma componente mais intensa na região espectral do verde e uma banda de menor intensidade relativa na zona do ultravioleta. Os espectros de fotoluminescência dos nanofios no substrato de Si foram analisados em detalhe a 12 K, mostrando diferentes componentes, tais como excitões ligados a dadores, pares aceitador-dador, réplicas de fonões de óptica longitudinal emissão associada a defeitos. Não foram identificadas transições de excitões livres, o que indica que os nanofios apresentam vários tipos de defeitos.

Keywords ZnO, nanostructure, thermal evaporation, supersaturation, nanowires, nanorods, photoluminescence.

Abstract

ZnO nanowires/nanorods have been synthesised by thermal evaporation on alumina (Al_2O_3) and silicon (Si) substrates. The morphology, crystal structure and optical properties of the as-grown nanowires/nanorods have been characterised by scanning electron microscopy (SEM), X-ray diffraction (XRD), and photoluminescence in excitation (PLE) and emission (PL) modes. The SEM images reveal that the morphologies of the nanowires/nanorods are very sensitive to the synthesis parameters such as temperature, substrate and flow rate of O_2 and N_2 gases. The nucleation and growth behaviour of the nanowires/nanorods are also discussed on the basis of vapour-solid growth mechanism. The XRD results show that the nanowires/nanorods have hexagonal wurtzite phase of bulk ZnO. The room temperature PL spectra consist of two emission bands, namely a dominant green luminescent band and a lower relative intensity band in the ultraviolet spectral region. The photoluminescence features of the nanowires on Si substrate have been analysed at 12 K. Different transition lines such as bound exciton, donor-acceptor pair, longitudinal optical phonon replicas and defect-related emissions have been observed. There is no clear observation of free exciton transition lines, indicating that the nanowires consist of several defects.

Table of Contents

Acknowledgment i
Abstract iii
List of abbreviations v
List of figures vi
List of tables viii
Outline of the thesis ix
Chapter 1: 1
1.1. Introduction 1
1.2. Properties and applications of ZnO 2
1.2.1. Crystal Structures and Surfaces 2
1.2.2. Piezoelectric Property 3
1.2.3. Optical Property 4
1.2.4. Electric and Magnetic Properties 4
Chapter 2: 5
2. Band Structure and Optical Transitions of ZnO 5
2.1. Band Structure 5
2.2. Absorption and Emission 7
2.3. Free Excitons 9
2.4. Defect Energy Levels in ZnO 11
Chapter 3: 16
3. Growth Techniques and Mechanisms of 1D Nanostructures 16
3.1. Thermal Evaporation Technique 16
3.2. Phase Diagram and Vapor Pressure of Zn 17
3.3. Growth Mechanisms 19
3.4. VLS Mechanism 19
3.5. VS Mechanism 20
3.6. Nucleation and Growth of Nanowires/Nanorods 22
Chapter 4: 25
4. Experimental Description and Characterisations 25
4.1. Experimental Description 25
4.2. Characterisations 27
4.2.1. SEM Images of Nanowires/Nanorods 27
4.2.2. X-ray Diffraction of Nanowires/Nanorods 37
4.2.3. Photoluminescence Properties of Nanowires/Nanorods 41
4.2.3.1. Photoluminescence spectra of Nanowires/Nanorods at Room Temperature . 42
4.2.3.2. Photoluminescence Spectra of Nanowires at Low Temperature (12 K) 48
Chapter 5: 57
5.1. Conclusions and Future Perspectives 57
References 61

List of abbreviations

Å	Angstrom
atm	Atmosphere
ABE	Acceptor bound exciton
A^oX	Exciton bound to a neutral acceptor
Al_2O_3	Alumina
BX	Bound exciton
CB	Conduction band
CVD	Chemical vapor deposition
DAP	Donor acceptor pair
DBE	Donor bound exciton
D^oX	Exciton bound to a neutral donor
eV	Electronvolt
fwhm	Full width at half maximum
FX	Free exciton
GL	Green luminescence
h	Planck's constant
JCPDS	Joint Committee on Powder Diffraction Standards
k	Boltzmann constant
LA	Longitudinal acoustic
LO	Longitudinal optical
MOCVD	Metal-organic chemical vapor deposition
MBE	Molecular beam epitaxy
mm Hg	Millimeter of mercury
O_i	Oxygen interstitial
O_{Zn}	Oxygen antisite
PL	Photoluminescence
PVD	Physical vapor deposition
sccm	Standard cubic centimetre per minute
SEM	Scanning electron microscopy
Si	Silicon
SLS	Solution-liquid-solid
TA	Transverse acoustic
TO	Transverse optical
TES	Two-electron-satellite
UV	Ultraviolet
VB	Valance band
VLS	Vapor-liquid-solid
VS	Vapor-solid
V_O	Oxygen vacancy
V_{Zn}	Zn vacancy
Xe	Xenon
XRD	X-ray diffraction
Zn_i	Zn interstitial
Zn_o	Zn antisite

List of figures

Fig. 1-1. Unit cell of wurtzite structure ZnO [18,23]……..3

Fig. 2-1. (a) Wurtzite energy band structure of ZnO, showing the conduction and valence band symmetries and degeneracies at the center of the first Brillouin zone,(Γ-point), in the presence of spin-orbit coupling and crystal-field interaction [22].

(b) General band structure at Γ-point for C_{6v} symmetry and polarization selection rule. ⊥and // mean that the transitions are dipole-allowed for **E** ⊥ **c** and **E** // **c**, respectively. Transitions by **E**⊥**c** and **E** // **c** are partially allowed for B and C excitons ((⊥) and (//)) [25]……..6

Fig. 2-2. Configurational Diagram for the ground state and one of the excited electronic states of a vibronic solid. The optical transitions are indicated by the vertical arrows. The right hand side of the figure shows the general shape of the absorption and emission spectra that would be expected , taken from [28] with slight modification……...8

Fig. 2-3. Emission spectrum of ZnO nanowires at 6ºK at excitation intensity of 596 kW/cm^2. The dotted lines are Gaussian fitting to the emission peaks [30]…….……...11

Fig. 2-4. Schematic diagram for the main transitions in a semiconductor: a) excitonic, b) electron-acceptor, c) donor to valance band, d) donor-acceptor, and e) band-to-band transitions….12

Fig. 2-5. Low temperature emission spectrum of ZnO rods, showing the different emission peaks [33]……..……..12

Fig. 2-6. Bound excitonic region of the 10 K emission spectrum for the forming gas annealed ZnO substrate [27]……...…….13

Fig. 2-7. Energy levels of defects in ZnO: a) the draft of the calculated defect´s level in ZnO thin films [34], b) Scheme of the UV emission and the three visible, yellow, green and blue, emissions in ZnO nanowires [40]……..……..……15

Fig. 2-8. Room temperature emission spectrum of ZnO nanowires grown on Si(100) substrate [35]…….……...14

Fig. 2-9. Emission spectrum at 4.8 K from an as-grown bulk ZnO sample, the intensity is shown in a logarithmic scale [39]…….……...14

Fig. 3-1. The horizontal tube furnace used for the growth of ZnO nanostructures……...……17

Fig. 3-2. Phase diagram of Zn……...……...……....……..…18

Fig. 3-3. Vapor pressure of liquid Zn……...…...……..……....18

Fig. 3-4. A) Schematic illustration showing the growth of a nanowire via the Vapor-liquid-solid (VLS) mechanism. B) The binary phase diagram between Au and Ge, with an indication of the compositional zones responsible for alloying, nucleation, and growth [49]……..……..20

Fig. 3-5. Schematic representation of total Gibbs free energy as a function of nucleus radius…...24
Fig. 3-6. Supersaturation profile of ZnO vapor in the reactor under different flow rate of carrier gas along the distance downstream from the source material, ref(115) in [57]……..24
Fig. 4-1. Schematic diagram of the experimental setup for the synthesis of ZnO nanostructures....26
Fig. 4-2. Temperature profile in the Al_2O_3 tube at furnace temperature of 720 ºC. I, II, III, and IV denote Substrate-I, Substrate-II, Substrate-III, and Substrate-IV, respectively.…….....…..26
Fig. 4-3. (a) SEM images of the nanorods grown on Si substrate, Substrate-I, (b) the magnified image…….28
Fig. 4-4. (a) SEM images of the nanowires grown on Si substrate, Substrate-II, (b) the magnified image……30
Fig. 4-5. SEM images of the nanowires grown on Al_2O_3 substrate, Substrate-I…….....…...…..31
Fig. 4-6. SEM images of the nanowires grown on Al_2O_3 substrate, Substrate-II….....……....32
Fig. 4-7. SEM images of nanowires grown on Al_2O_3 substrates: (a) on Substrate-II with N_2 flow rate 350 sccm, (b) on Substrate-I with N_2 flow rate 450 sccm.……35
Fig. 4-8. XRD patterns of samples on Al_2O_3 and Si substrates and diffraction peaks of the substrates: a) nanowires on Al_2O_3 substrate (Substrate-II) grown with O_2 and N_2 flow rates 100 and 450 sccm, respectively, b) nanowires on Al_2O_3 substrate (Substrate-I) grown with O_2 and N_2 flow rates 100 and 350 sccm, respectively, c) nanorods on Si substrate (Substrate-I) grown with O_2 and N_2 flow rates 80 and 450 sccm, respectively, d) nanowires on Si substrate (Substrate-II) grown with O_2 and N_2 flow rate 100 and 450 sccm, respectively, e) Al_2O_3 substrate, f) Si substrate. The peaks marked by * are from ZnO.…….……38
Fig. 4-9. XRD pattern showing relative intensity differences between peaks of the nanowires (blue color) on Si substrate grown with O_2 and N_2 flow rates 100 and 450 sccm, respectively, nanorods (red color) on Si substrate grown with O_2 and N_2 flow rates 80 and 450 sccm, respectively, and nanowires (black color) on Al_2O_3 substrate grown with O_2 and N_2 flow rates 100 and 450 sccm, respectively.……...……....40
Fig. 4-10. Schematic Diagram of the photoluminescence setup……...……...…….42
Fig. 4-11. Room temperature excitation spectra of the (a) nanorods on Si substrate, (b) nanowires on Si substrate and (c) nanowires on Al_2O_3 substrate, the emission wavelengths being monitored between 464 and 565 nm…….……43
Fig. 4-12. Room temperature emission spectra of the (a) nanorods and (b) nanowires on Si substrate, excited at 280 nm (black color), 334 nm (green color), 360 nm (red color) and 375 nm (blue color)……..44
Fig. 4-13. Room temperature emission spectra of nanowires on Al_2O_3 substrate, excited at 280 nm (black color), 300 nm (red color) and 330 nm (green color)……....44

Fig. 4-14. Room temperature emission spectra of the (a) nanowires and (b) nanorods on Si substrate, excited at 312 nm (3.94 eV)…….....47
Fig. 4-15. Low temperature (12 K) excitation spectra of ZnO nanowires on Si substrate, the emission wavelengths being monitored at 366 nm (red color), 374 nm (green color), 420 nm (black color) and 500 nm (blue color)…….……...……..48
Fig. 4-16. Low temperature (12 K) emission spectra of nanowires on Si substrate, excited at different wavelengths: 240 nm (green color), 305 nm (blue color), 334 nm (red color), 365 nm (black color)……..49
Fig. 4-17. Emission spectra of nanowires on Si substrate at 12 K, excited at 316 nm (blue color) and 334 nm (green color)…….…50
Fig. 4-18. Room temperature and low temperature emission spectra of the nanowires on Si substrate, excited at 334 nm (3.71 eV)…...……..51
Fig. 4-19. Room temperature and low temperature emission spectra of the nanowires on Si substrate, excited at 365 nm (3.40 eV)……...…….…….54

List of tables

Table-1 Parameters Pertinent to ZnO, ref(4) in [19]..…….7
Table-2 Summary of the experimental results……...36

Outline of the thesis

This thesis consists of five chapters classified and organized in a logical manner. Chapter 1 provides a general overview about some properties of nanostructures, in particular to one dimensional zinc oxide (ZnO) nanostructures. In this chapter, the crystal structure, piezoelectric, optical, electrical and magnetic properties, and some applications of ZnO will also be highlighted. In chapter 2, the basics of semiconductor physics such as band structure and optical transitions in ZnO will be briefly described to support the discussion and analysis on the photoluminescence of the nanowires/nanorods in chapter 4. Chapter 3 presents the synthesis methods for one dimensional (1D) nanostructures in general and thermal evaporation method for the growth of ZnO nanowires/nanorods in particular. The phase diagram and vapor pressure of zinc (Zn) will be presented to understand the thermal evaporation process of Zn and the two vapor phase growth mechanisms, namely, Vapor-Liquid-Solid (VLS) and Vapor-Solid (VS). Based on the characteristics of VLS and VS growth mechanism, the nucleation and growth of nanowires/nanorods have been proposed. In chapter 4, the experimental description of the thermal evaporation method used in this work and the characterisation of the as-grown nanowires/nanorods are presented. Finally, conclusions and future outlooks of the work are briefly presented in Chapter 5.

Chapter 1:

1.1. Introduction

The development of nanoscience and nanotechnology has come up with a number of nanostructures with novel properties which are not found in nature. The novel properties of such structures result from the effects of quantum confinement and large ratio of surface area to volume relative to the bulk counter parts. The idea behind quantum confinement is keeping charge carriers in a small area so that the carriers can be confined by potential barriers in one, two or three dimensions, named as quantum films or quantum wells, quantum wires and quantum dots, respectively, [1-3]. A quantum well is a thin film of macroscopic width and length which frees the carrier to move in a plane and bounds it in the third direction. Thus, it is said to be confined in one dimension (1D). Quantum wires, which are confined in two dimensions (2D), can be thought of as nanometer-sized cylinders that can measure up to several microns in length. Likewise, a quantum dot is a nanometer-sized sphere/box confined in all three dimensions (3D). Because of these confinement effects and large area to volume ratios materials including semiconductor nanostructures can display novel features such as electrical, optical, mechanical and thermal properties which might be different from bulk semiconductors of the same composition. In particular, the confined dimensions result in a quantization of the bulk electronic bands and a widening of the band gap energy between the valence band and conduction band, which is size dependent.

Due to their importance in basic scientific research and possible technological applications, one dimensional (1D) structures with nanometer size, nanowires/nanorods, have great potential to study the dependence of the aforementioned novel properties on the size and dimension of semiconductor materials [3,4,5]. They are expected to be used both as interconnects and functional components in the fabrication of nanoscale electronic and optoelectronic devices. Consequently, among the wide ranges of semiconductor materials, ZnO has been found to be the richest family of oxide nanostructured materials and received an immense attention due to its attractive properties and potential device applications in electronic, photonic, optoelectronic, piezoelectric, chemical sensor and spintronic devices [6,7,8,9]. It is a direct, wide band gap, n-type, wurtzite structured and II-VI compound

semiconductor with band gap energy and exciton binding energy of 3.37 eV and 60 meV at room temperature, respectively. As a result, fundamental investigations on the properties of ZnO nanostructures are essential for the advancement of nanoscale device fabrication.

Objectives of the study:

- To synthesise ZnO nanowires/nanorods on silicon (Si) and alumina (Al_2O_3) substrates by a simple thermal evaporation method at ambient pressure without using any catalyst or additive.
- To characterise the as-grown nanowires/nanorods with scanning electron microscopy (SEM), X-ray diffraction (XRD) and photoluminescence (PL) spectroscopy.

1.2. Properties and applications of ZnO

As mentioned above, ZnO is a semiconductor which can be used for different novel applications. To understand more about the growth behaviours and applications of this semiconductor, it is worth to discuss on some of its fundamental properties and applications. Hence, properties like crystal structure, piezoelectric, optical, electrical, and magnetic will be introduced in the following sections, the former being the determining factor for most of the properties.

1.2.1. Crystal Structures and Surfaces

Among the three possible crystal structures of ZnO, wurtzite, zinc blende, and rock salt, the wurtzite crystallized ZnO is a thermodynamically stable form of ZnO under ambient conditions. It has a hexagonal unit cell with lattice parameters a=3.296 Å and c=5.206 Å and belongs to the space group of C^4_{6v} or $P6_3mc$ [7]. Schematically, the hexagonal wurtzite structure of ZnO can be described as alternately stacked planes of tetrahedrally coordinated O^{2-} and Zn^{2+} ions along the c-axis as shown in Fig. 1-1. Such coordination of ZnO results in non-central symmetry structure which eventually gives ZnO an inherent property of piezoelectricity and pyroelectricity [9]. Another important characteristic of ZnO is its polar surfaces. The oppositely charged ions produce positively charged Zn-(0001) and negatively charged O-$(000\bar{1})$ surfaces resulting in a dipole moment and spontaneous

polarization along c-axis as well as divergence in surface energy along the different crystallographic directions [6]. Generally, the divergence in surface energy causes instability in the crystal structure and hence the different polar surfaces exhibit immense surface reconstructions to maintain stable structure depending on the processing conditions. However, the ± (0001) polar surface is observed to be atomically flat and stable without any surface reconstruction [9]. From the point of view of growth, the wurtzite ZnO has three types and a total of 13 fastest growth directions, $\langle 0001 \rangle$, $\langle 01\bar{1}0 \rangle$ and $\langle 2\bar{1}\bar{1}0 \rangle$ [5,10]. As a result, together with its polar surfaces, ZnO has been demonstrated to exhibit a wide range of novel nanostructures such as nanowires, nanorods, nanoneedles, nanorings, nanosprings, nanocombs, nanotubes, nanohelixes, nanobelts and nanocages that can be grown by controlling the growth rates along these directions [5,6,7,10,13].

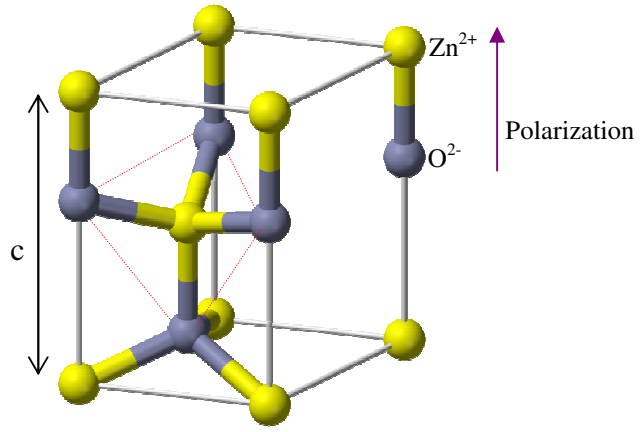

Fig. 1-1. Unit cell of wurtzite structure ZnO [18,23].

1.2.2. Piezoelectric Property

In relation to the crystal structure, one of the important properties of ZnO is its piezoelectricity which has been extensively studied for various applications in force sensing, acoustic wave resonator, acoustic-optic modulator etc [8,11]. The origin of piezoelectricity lies in the absence of non-inversion symmetry of the tetrahedrally coordinated oxygen and Zn ions in a ZnO molecule. Applying an external pressure displaces the centre of positively and negatively charged ions by inducing a distortion of lattice. These displaced charges result in local dipole moments which will grow to net macroscopic dipole moment on the global crystal. It was reported that ZnO nanowires have high piezoelectric constant (d_{33}=246) which makes it an interesting material for the application in mechanical devices such as acoustic transducers, sensors and actuators [15].

1.2.3. Optical Property

The optical properties of a material are directly in touch with the band gap energy and band structure, which in turn depend on the crystal structure of the material. Hence, because of its wide direct band gap and large exciton binding energy, ZnO is an excellent candidate semiconductor material compared to other known wide band gap materials such GaN and SiC for optical applications [13,39]. It can be used in UV nano-optoelectronics and lasers which operate at room temperature [8,15]. This is due the fact that its exciton binding energy (60 meV) is by far greater than the thermal energy (~26 meV) at room temperature, compared to the exciton binding energy of other semiconductors known for their wide band gap such as GaN (exciton binding energy ~25 meV) [4].

1.2.4. Electric and Magnetic Properties

The future applications of ZnO for nano-electronics need fundamental study of the electrical properties of ZnO nanostructures. Due to the native defects such as oxygen vacancies and Zn interstitials (section 2.4), the as-grown ZnO nanowires are reported to show n-type semiconductor behaviours [11]. Electrical transport measurements such as conductivity and resistivity were preformed on a single ZnO nanowire/nanorod by configuring it as field effect transistors (FETs) following several procedures [14]. The important issue observed here is that the superior electrical property that single crystalline ZnO nanowires render as compared to the polycrystalline ZnO thin films. For instance, an electron mobility of 7 cm^2/V s is regarded as quite high for ZnO thin film transistors, ref(12) in [11]. But, Chang et al. [15] have shown that a single crystalline ZnO nanowire has mobility as high as 80 cm^2/V s. Park et al. [12] have also reported ZnO nanorod FETs with a high transconductance of 1.9 μS and high electron mobility of 1000 cm^2/V s, after coating the nanorods with polyamides. These results indicate that ZnO based nanoscale devices can achieve a faster operation speed than the thin film counterparts. In additions, ZnO has been considered for spintronic applications because of the reason that it is a promising host material for ferromagnetic doping. Using manganese, Mn, as dopant, the ferromagnetic ordering of ZnO was predicted theoretically and confirmed experimentally [11,14]. Substituting 13% of Zn in ZnO by manganese, Chang et al. [16] have succeeded in growing ferromagnetic $Zn_{1-x}Mn_xO\,(x = 0.13)$ nanowires with Curie temperature of 37 K.

Chapter 2:

2. Band Structure and Optical Transitions of ZnO

Semiconductors have a band structure which can be filled with various allowed energy states of which some are localized due to impurities or defects and the others such as excitons move through the crystal. The optical properties of semiconductors are thus the effect of transitions of carriers between these energy states. Hence to have a better understanding and analysis on the characterisations of ZnO nanowires and nanorods, first it is fundamental to review the basics of semiconductor physics, such as band structure, band gap, defect levels in the band gap, absorption and emission. The following sections present these concepts briefly.

2.1. Band Structure

Bands of energy states are formed when the constituent atoms of a solid approach each other and the wave functions of their electrons begin to overlap. Even though it is not straightforward to calculate the exact band structure of a real crystal, the existence of energy bands and band gaps (forbidden energy regions) can be demonstrated using some models such as the nearly free electron model [17,28]. Accordingly, it is found that there are two types of energy bands separated by an energy gap in a solid, the lower band states known as the valance band (VB) whereas the upper band states known as conduction band (CB). In fact, the extent of the energy gap and the relative availability of charge carriers (electrons or holes) within the bands classify materials as a metal, a semiconductor or an insulator and thus determine their optical (electrical) properties and device applications. In metals the energy gap is either very small or no energy gap exists at all. In semiconductors the energy gap may extend to less than 4 eV (e.g., 3.37 eV for ZnO at room temperature) whereas insulators have very wide energy gap compared to metals and semiconductors.

It is common to represent the conduction and valance bands with energy-momentum diagram, E(**k**) versus **k**, where **k** is the wave vector, which makes simple to describe the conservation of both energy and momentum in the absorption, reflection or emission processes. In the energy-momentum diagram, the valance band of ZnO near **k**=0 consists of three subbands named as A, B and C which are separated by spin-orbit and crystal-field

interactions as in Fig. 2-1, even though there are controversies in the symmetry orderings between A and B subbands. Some researchers argue for the symmetry ordering of A-Γ_9, B-Γ_7, C-Γ_7 [19,22,25,27] whereas others support the inverted ordering A-Γ_7, B-Γ_9, C-Γ_7 [20,23,24], detailed explanations and arguments can be found in the references [20,21,23]. The valance and conduction bands are p-like states of O and s-like states of Zn, respectively, [19-24,26,27]. Thus, the fundamental optical transitions can happen between the subbands and the conduction band depending on the selection rules. For instance, in the δ-polarization geometry where the electric field (**E**) is perpendicular to the c-axis (**c**), **E**$\perp$**c**, the A and B-transitions are strongly allowed but the C-transition is partially allowed (Fig. 2-1b). In the absorption or photoluminescence (PL) spectra, a direct transition between the top of valance band and the bottom of conduction band can be accompanied by small peaks or steps at slightly higher energies that correspond to transitions between conduction band and the lower subbands [29]. Different spectroscopy techniques including photoluminescence have been used to measure the transition lines of A, B and C excitons which will be discussed in the next sections. Table-1 presents typical experimental data measured at 2 K with PL and reflectance spectroscopes for the A, B and C exciton lines of high quality ZnO samples grown by physical vapor transport method [19]. The band structure and allowed exciton transitions of wurtzite ZnO near **k**=0 are shown in Fig. 2-1.

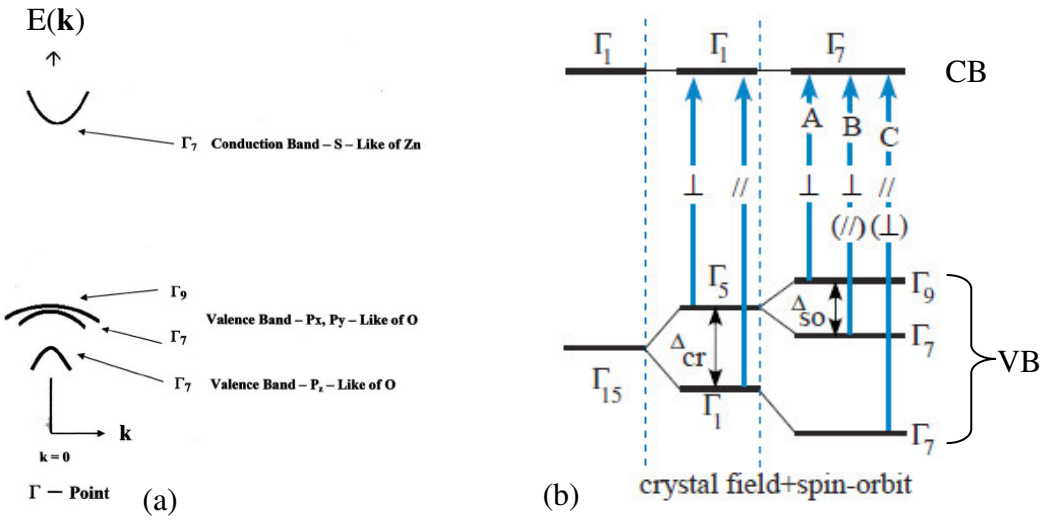

Fig. 2-1. (a) Wurtzite energy band structure of ZnO, showing the conduction and valence band symmetries and degeneracies at the center of the first Brillouin zone,(Γ-point), in the presence of spin-orbit coupling and crystal-field interaction [22].
(b) General band structure at Γ-point for C_{6v} symmetry and polarization selection rule. $\perp$ and // mean that the transitions are dipole-allowed for **E** $\perp$ **c** and **E** // **c**, respectively. Transitions by **E**$\perp$**c** and **E** // **c** are partially allowed for B and C excitons (($\perp$) and (//)) [25].

Table-1 Parameters Pertinent to ZnO, ref(4) in [19].

Parameters	Values	Measured PL-Spectra	Derived
A-Exciton Γ_5 Ground-State Energy	3.3773 eV	*X*	
$n=2$ energy	3.4221 eV	*X*	
$n=3$ energy	3.4303 eV	*X*	
Binding Energy $n=2$	0.0597 eV		*X*
Binding Energy $n=3$	0.0596 eV		*X*
Band Gap Energy	3.4370 eV		*X*
A-Exciton Γ_6 Ground-State Energy	3.3756 eV	*X*	
$n=2$ Energy	3.4209 eV	*X*	
$n=3$ Energy	3.4288 eV	*X*	
Binding Energy $n=2$	0.060 eV		*X*
Binding Energy $n=3$	0.0598 eV		*X*
B-Exciton Ground-State Energy	3.3895 eV	*X*	
$n=2$ Energy	3.4325 eV	*X*	
Binding Energy	0.057 eV		*X*
Band Gap Energy	3.4465 eV		*X*
$E_{AB}, \Gamma_9-\Gamma_7$	0.0095 eV		*X*
Parameters	Values	Measured Reflection Spectra	Derived
A-Exciton Reflection Minima	3.3776 eV	*X*	
B-Exciton Reflection Minima	3.3938 eV	*X*	
C-Exciton Reflection Minima	3.4335 eV	*X*	
$E_{BC}, \Gamma_7-\Gamma_7$	0.0397 eV		*X*
Spin-Orbit Parameter	0.016 eV		*X*
Crystal-Field Parameter	0.043 eV		*X*

2.2. Absorption and Emission

In the absorption process, a photon of known energy excites an electron from the lower energy state where it would be in equilibrium to the higher one provided that the photon energy is at least equal to the energy difference between the two states. On the other hand, an electron occupying a higher energy state which is usually a non-equilibrium state makes a transition to the lower energy state in a radiative (emission of photons) or non-radiative ways. The energy of absorption and emission will be the same only when vibrational (rotational) excited states are not involved in the transitions [28]. However, the vibrational states of a molecule change during electronic transitions and hence there is coupling of vibrational and electronic transitions. Similarly, in semiconductors, electrons trapped to defect or doped impurity atoms can also couple to the vibrational modes of the host crystal by electron-phonon interaction and give rise to absorption and emission bands as shown schematically in the right hand side of Fig. 2-2. This mechanism can be illustrated using a simple 1D model diagram known as Configuration Diagram which presents the energy of

the ground state and first excited state of an atom as a function of its position, x, [28,29]. The equilibrium positions of the ground and the excited states, x_o and x´, respectively, are displaced according to the strength of the electron-phonon interaction. The model follows the ***Born-Oppenheimer (or "adiabatic") approximation*** which assumes the electronic transitions are vertical or almost vertical lines as the electronic transition occurs so rapidly that the atom can not change its position during such transition [28].

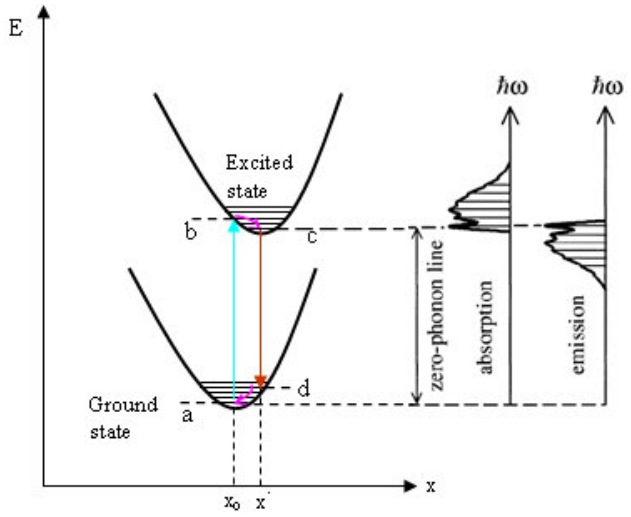

Fig. 2-2. Configurational Diagram for the ground state and one of the excited electronic states of a vibronic solid. The optical transitions are indicated by the vertical arrows. The right hand side of the figure shows the general shape of the absorption and emission spectra that would be expected, taken from [28] with slight modification.

Accordingly, at equilibrium position, x_o, the ground state of the atom is assumed to be at its lowest vibrational level. Photoexcitation of the atom promotes the electron to the excited state without changing the equilibrium position of the atom, transition $a \rightarrow b$ in Fig. 2-2. The electron then relaxes to the lowest vibrational level of the excited state by releasing the excess energy as phonons, transition $b \rightarrow c$ in Fig. 2-2. During this relaxation, the excited state changes its equilibrium position to x´ which is slightly at a different lattice coordinate of the atom. The electron returns to the ground state by emission of photon without altering the equilibrium position x´ of the excited state, transition $c \rightarrow d$ in Fig. 2-2. Finally, the system relaxes to the zero level of the ground state by the emission of several phonons, transition $d \rightarrow a$ in Fig. 2-2. Transition from the lowest vibrational level of the ground state to that of the excited state, $a \rightarrow c$, is called the zero-phonon line where the absorption and emission lines occur at the same frequency. In general, the energy emitted

in transition $c \rightarrow d$ is lower than the energy absorbed in transition $a \rightarrow b$. The energy difference between the two transitions is called ´´Stokes shift´´ [29].

The electron-phonon coupling strongly depends on temperature. As the temperature of a semiconductor increases, the lattice expands and the oscillation of the atoms about their equilibrium lattice points increases, more phonons being involved in the coupling. Moreover, wurtzite ZnO has 4 atoms per unit cell and hence a total of 12 phonon modes; six transverse optical (TO) modes, two transverse acoustic (TA) modes, three longitudinal optical (LO) modes, and one longitudinal acoustic (LA) modes.

2.3. Free Excitons

As mentioned above, the absorption of a photon in a semiconductor could create an electron in the conduction band and a hole in the valance band. The electron and the hole can attract to each other through their mutual coulomb interaction and form an electron-hole pair called exciton. A free exciton (FX) is a free electron-hole pair held by the coulomb attraction. In the simplest picture, the binding energy E_x of such a system is given by the Bohr model in which the electron orbits about the hole as if it were hydrogen like atom [29]

$$E_x = \frac{-m^* e^4}{2h^2 \varepsilon^2 n^2} \qquad (1)$$

where $n = 1, 2, 3, ...$ is the quantum number of various states, e is the electron charge, ε is the dielectric constant and $m^* = \frac{m_e^* m_h^*}{m_e^* + m_h^*}$ is the reduced mass of the exciton, m_e^* and m_h^* being the electron and hole effective masses, respectively.

Since the electron and hole of an exciton move together through the semiconductor, their group velocities must be the same. This can be satisfied during a direct transition at **k**=0 indicating that strong excitonic transitions are expected in the spectral regions close to the fundamental band gap energy E_g of the semiconductor. Thus the photon energy hv, v and h being the frequency and Planck's constant respectively, required for the formation of an exciton during a direct transition near the Γ point is given by the conservation of energy

$$hv = E_g - E_x \qquad (2)$$

Using the effective mass approximation, equation (1) helps to predict the exciton binding energy and then the band gap energy of the semiconductor. However, free excitons are formed easily only for the purest samples and at low temperatures [28]. In samples with high concentration of impurities or defects, the coulomb interaction in the excitons can be screened (the binding force of the exciton is strongly reduced) by the free electrons and holes released from the impurities. Moreover, excitons might be ionized by electric fields generated by charged impurities. Excitons are also ionized at high temperatures when the thermal energy kT, where k is Boltzmann constant and T is temperature, is greater than the binding energy of the excitons. On the other hand, excitons can be bound to an impurity or a defect to form bound excitons (BX) which are in fact the dominant transition lines in the emission spectra of bulk and nanostructured ZnO as supported by many PL studies [20,21,27,30] (Fig. 2-3).

Hence it is only for high quality ZnO samples, usually at low temperatures, that the three free exciton lines discussed in section 2.1 can be observed in the absorption, PL and reflectance measurements (Table-1). Temperature dependent photoluminescence is one of the most widely used techniques to investigate the free exciton transition lines in ZnO [24-27,30,34,41]. Such investigations have enabled to measure the free exciton and their excited state energies, the binding energies, the band gap energy E_g, the spin-orbit and crystal-field interaction energies (as in Table-1). In addition, it is possible to investigate the exciton-phonon interactions from the exciton energy obtained at various temperatures because the band gap energy E_g can be perturbed by the temperature and for most semiconductors it is given by Varshni empirical formula [31]

$$E_g(T) = E_g(0) - \frac{\alpha T^2}{T + \beta} \qquad (3)$$

where $E_g(T)$ and $E_g(0)$ are the values of the energy gap at a given temperature T and 0 K, respectively, and α and β are constants.

Equation (2) is true in the assumption that phonons are not involved in the exciton transitions. However, as it has been observed experimentally [21,27,30], the free exciton transition may couple with the emission of one or more longitudinal optical phonons in

which case the narrow emission spectrum of the free excitons can be replicated at several lower photon energies given by [29]

$$hv = E_g - E_x - mE_p \qquad (4)$$

where m is the number of optical phonons emitted per transition and E_p is the energy of phonon involved. For instance, the A-free exciton phonon replicas have been observed in room temperature and low temperature emission spectra of ZnO nanowires [30]. Fig. 2-3 shows a typical emission spectra showing a dominant bound exciton (BX) line, the A-free exciton ($FX_A^{n=1}$), and its first excited state ($FX_A^{n=2}$), first, second and third order longitudinal phonon replicas, ($FX_A^{n=1} - mLO$), for ZnO nanowires at 6 K.

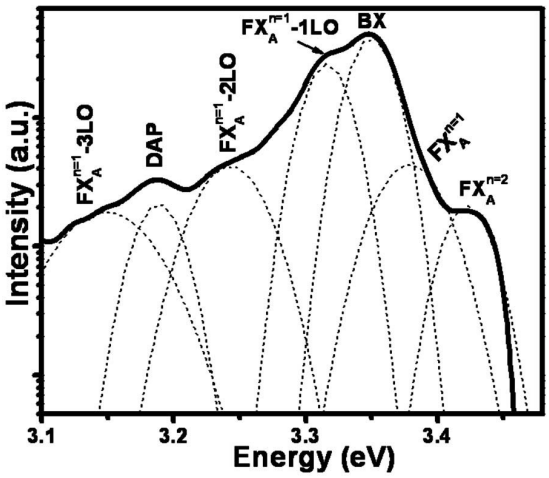

Fig. 2-3. Emission spectrum of ZnO nanowires at 6 K, at excitation intensity of 596 kW/cm^2. The dotted lines are Gaussian fitting to the emission peaks [30].

2.4. Defect Energy Levels in ZnO

The presence of intrinsic and/or extrinsic defects in a semiconductor usually introduces discrete energy levels in the band gap and thus potentially affects the transition processes [27]. These levels may be due to a neutral (charged) donor, acceptor or both of them. Like electron-hole pair, a donor and an acceptor can also form a pair called donor-acceptor pair (DAP) which is localized in the host semiconductor. Therefore, a DAP transition will occur if the photon energy is equal to the pair interaction energy E_{pair} between the acceptor and the donor levels according to the relation [29], in the absence of phonons.

$$E_{pair} = E_g - E_D - E_A + \frac{e^2}{\varepsilon R} \qquad (5)$$

where E_g, E_D , E_A , ε , e , and R are the band gap energy, donor binding energy, acceptor binding energy, dielectric constant, electron charge and donor-acceptor pair distance, respectively.

As a result of the space dependent coulomb interaction between the acceptor and the donor in equation (5), several DAP transitions can be expected (Fig. 2-5). For distant pairs the coulomb interaction term is very small and the photon energy will be smaller. On the other hand, shorter distant pairs experience strong coulomb interactions and contribute to the spectral lines at higher photon energies close to E_g. Hence, the spectral features of DAP transition lines are determined by the coulomb interaction, the pair separation.

In general, transitions between the conduction band and a donor or between the valance band and an acceptor are considered as shallow transitions while deep transitions are those between a donor level and the valance band and between the conduction band and an acceptor level. Fig. 2-4 shows the schematic diagram of the main transitions in a semiconductor containing defect energy levels.

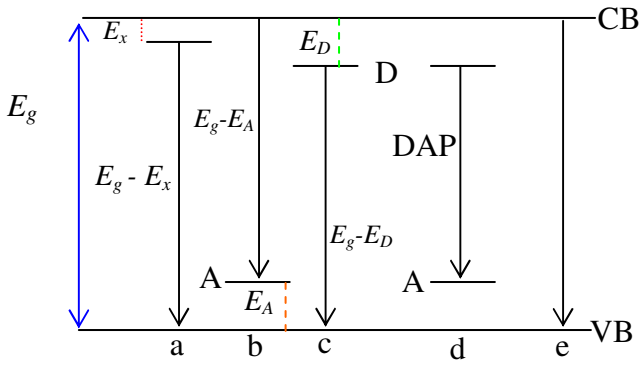

Fig. 2-4. Schematic diagram for the main transitions in a semiconductor: a) excitonic, b) electron-acceptor, c) donor to valance band, d) donor-acceptor, and e) band-to-band transitions.

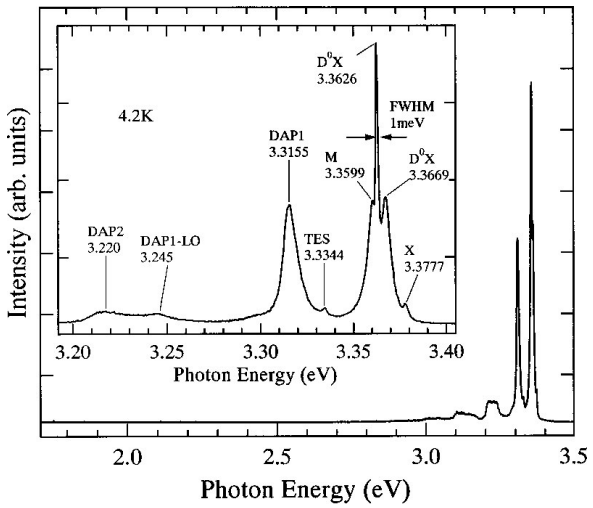

Fig. 2-5. Low temperature emission spectra of ZnO rods, showing the different emission peaks [33].

Furthermore, an exciton could be bound to a neutral/charged donor and acceptor to form a donor bound exciton (DBE) and an acceptor bound exciton (ABE), respectively. Hence several transition lines of the bound excitons such as the neutral donor bound exciton (D^oX), the A exciton bound to a neutral donor (D^oX_A) and a neutral acceptor (A^oX_A), and their excited state have been observed in the low temperature emission spectra of bulk and nanostructured ZnO samples. Fig. 2-6 shows a typical bound exciton region of bulk ZnO sample at 10 K.

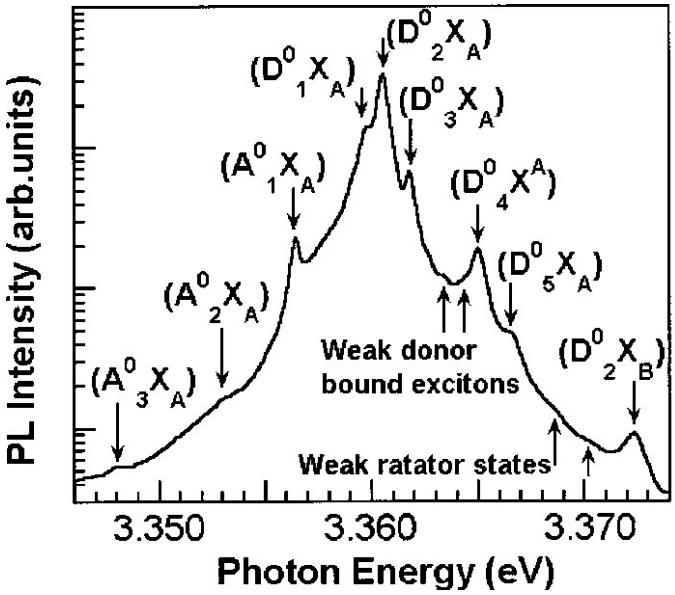

Fig. 2-6. Bound excitonic region of the 10 K emission spectrum for the forming gas annealed ZnO substrate [27].

Another transition line, as in Fig. 2-5, might occur when an exciton bound to a neutral donor recombines radiatively and leaves the donor in its excited states, 2s, 2p, known as two-electron-satellites (TES) lines. The energy separation between the ground state neutral donor bound exciton (D^oX) and its excited state (TES) lines is considered as the difference between the donor energies in the 1s and 2p states and it is ¾ of the donor binding energy E_D, in the effective-mass approximation [20,21,27]. This can help to estimate E_D from the position of TES and D^oX transition lines in the emission spectrum.

The presence of native defects resulting from oxygen and Zn vacancies (V_O and V_{Zn}), interstitials (O_i and Zn_i), and antisites (O_{Zn} and Zn_O) in ZnO has been calculated theoretically and confirmed experimentally [26,34]. It has been also reported that these

defects can be in complex forms such as $V_{Zn}V_o$ and V_oZn_i. Of the experimental techniques, PL spectroscopy is the most widely used technique to identify defect emissions in the band gap of both bulk and nanostructured ZnO [30,32,35-39]. However, there are controversies on the assignment of defect energy levels in the band gap as well as on the chemical origin of the emission peaks in the observed emission spectra. One of the arguments is on the most commonly observed green emission. For instance, L. Yang et al. [35] have observed a relatively weak UV peak followed by a dominant green emission band with a broad feature (420-600 nm) in the room temperature emission spectrum of ZnO nanowires grown on Si(100) substrate (Fig. 2-8). They proposed that the green emission is due to the recombination of a photogenerated hole with an electron in single ionized oxygen vacancy (V_O^+) resulted from the processing conditions. Many other research groups have also proposed oxygen vacancies being the source of green luminescence [39,40] contrary to Zn vacancies being the origin of the observed green emission in the work of A. Janotti and C. G. Van de Walle [26]. On the other hand, B. Lin et al. [34] have investigated the emission spectra of undoped ZnO films grown on Si substrates and calculated the defect levels using full potential linear musffin-tin orbital. They have concluded that the green emission peaking at 2.38 eV is due to the oxygen antisite (O_{Zn}) rather than V_o, V_{Zn}, Zn_i, and O_i (Fig.2-7a). In general, contradictory hypothesises have been reported for the origins of visible emissions because different defect types have been proposed to explain the same emission or the same defect type has been proposed for different emissions. Hence, no consensus has been established for the chemical origin of defect related emissions in ZnO though extensive photoluminescence investigations have been reported [32,36]. Fig. 2-7 shows some of the theoretically calculated energy levels and the proposed specific defects responsible for the visible emissions in ZnO. Fig. 2-9 presents typical emission spectrum of bulk ZnO sample at low temperature, showing the green and UV bands.

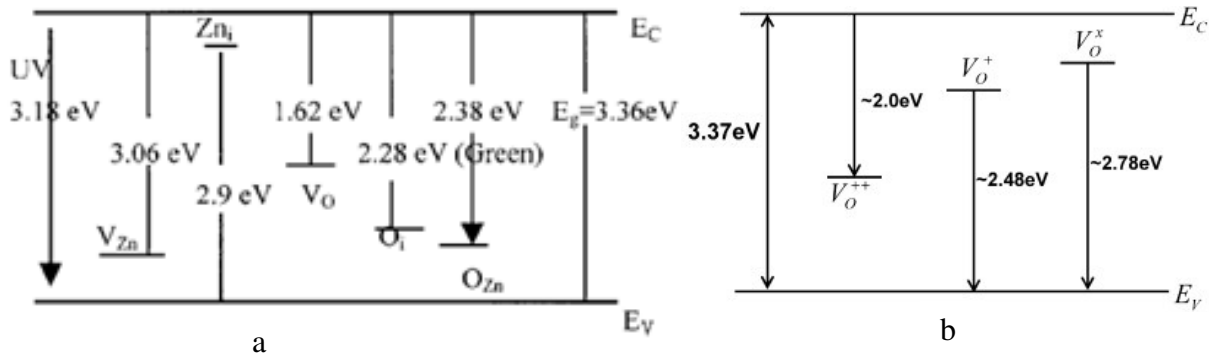

Fig. 2-7. Energy levels of defects in ZnO: a) the draft of the calculated defect´s level in ZnO thin films [34], b) Scheme of the UV emission and the three visible, yellow, green and blue, emissions in ZnO nanowires [40].

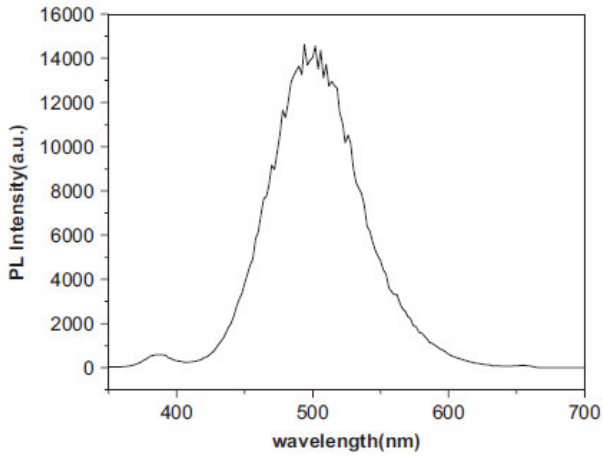

Fig. 2-8. Room temperature emission spectrum of ZnO nanowires grown on Si(100) substrate [35].

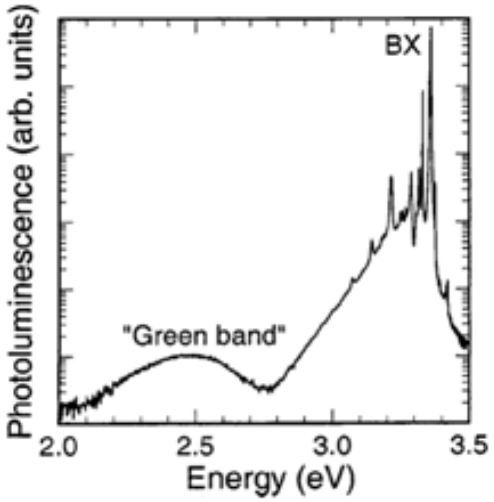

Fig. 2-9. The emission spectrum at 4.8 K from an as-grown bulk ZnO sample. The intensity is shown in a logarithmic scale [39].

Chapter 3:

3. Growth Techniques and Mechanisms of 1D Nanostructures

In the past few years, several fabrication techniques including chemical vapor deposition (CVD), molecular beam epitaxy (MEB) and electrodepostion methods have been used to synthesise 1D ZnO nanostructures. For example, S. W. Kim et al. [41] have synthesised ZnO nanowires by metal-organic chemical vapor deposition (MOCVD) using colloidal gold nanoparticles as a catalyst, Y. C. Kong and co-workers [42] demonstrated the synthesis of UV-emitting ZnO nanowires by physical vapor deposition (PVD) approach, the studies in [43] and [44] used CVD to synthesise catalytic growth of ZnO nanoneedles and nanowires respectively, L. Vayssieres [45] and S. Bu et al. [46] reported growth of arrayed nanorods and nanowires of ZnO from aqueous solutions, A. M. Morales and C. M. Lieber [47] used laser ablation method for the synthesise of silicon and germanium semiconductor nanowires. However, most of the techniques mentioned above are not simple to carry out the synthesis and they need selection of appropriate metal catalysts or additives which in turn contaminate the nanostructures and thus potentially change their final properties. Therefore, besides the motivation with the wide applications of ZnO nanostructures, a synthesis method which is simple, cost effective and reproducible is required. Accordingly, thermal evaporation technique has received increasing attention to synthesise varieties of oxide nanostructures such as nanowires, nanorods, nanotubes, nanorings, nanocombs, and nanotetrapods [2-6]. The basic features of thermal evaporation method will be introduced as follow.

3.1. Thermal Evaporation Technique

In thermal evaporation, the source material is vaporised at a temperature which is usually above the melting point of the material and then the resulting vapor phase is transported to the lower temperature regions for condensation onto the surfaces of the substrates under certain conditions (e.g., temperature, pressure and atmosphere). As it has been mentioned above, simply by changing the source martial, substrate type, source and substrate temperature various nanostructures of ZnO have been successfully synthesised using thermal evaporation method. Fig. 3-1 shows the horizontal tube furnace for the synthesis of ZnO nanowires, nonorods, nanoneedles, tetrapods, nanosheets and nanoplatlates in this

work. It mainly consists of a horizontal tube furnace with resistive heating elements, an alumina tube of length 50.0 cm and inner diameter 3.1 cm, 7 sets of thermocouples to record the temperature gradient in the alumina tube, gas inlet and outlet (See the schematic diagram of Fig. 4-1 for the detail).

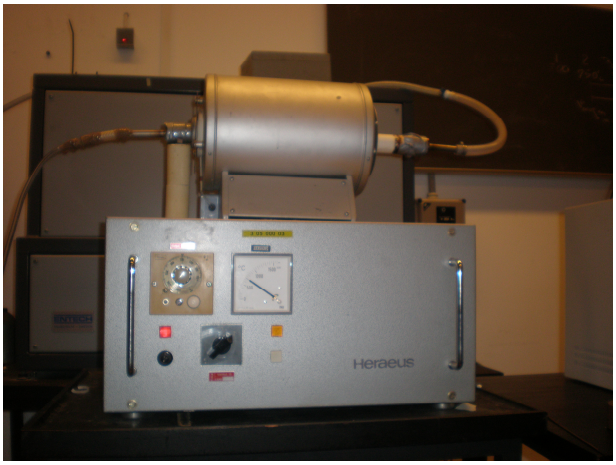

Fig. 3-1. The horizontal tube furnace used for the growth of ZnO nanostructures.

3.2. Phase Diagram and Vapor Pressure of Zn

It has been observed that temperature plays a key role on the morphologies and qualities of the final product. The amount of vapor from the source material, zinc (Zn), is determined by the temperature which is above the melting point (692.6 K) of Zn. Hence, knowledge about the relation between vapor pressure of Zn and temperature is essential for selecting optimal processing parameters such as temperature, oxygen concentration and distance of substrates from the source. Such relation can be determined from the principles of equilibrium thermodynamics which provides an equation for pressure, p, as a function of temperature T, $p = p(T)$. Referring to the thermodynamic table in [48], the vapor pressure of solid Zn varies with temperature as

$$\ln(p) = -\frac{15772.708}{T} - 0.755\ln(T) + 25.881, \text{ for } 273\ K \le T \le T_m \qquad (6)$$

and that of the liquid Zn varies as

$$\ln(p) = -\frac{15243.113}{T} - 1.255\ln(T) + 28.413, \text{ for } 693\ K \le T \le T_b \qquad (7)$$

where p is the vapor pressure in mm Hg, T_m and T_b being the melting and boiling point temperatures, respectively.

From these equations the triple point temperature, the boiling temperature and the equilibrium vapor pressure of Zn at a temperature of interest can be determined. Schematic representation for the phase diagram of Zn is depicted as in Fig. 3-2. From equation (6) and (7) the normal boiling temperature of liquid Zn is 1181 K (the temperature at which the vapor pressure of the liquid equals 1 atm) while the triple point temperature is 708 K. According to equation (6) the maximum vapor pressure that we can get from solid Zn is about 0.155 mm Hg ($2x10^{-4}$ atm) at a temperature of 691.5 K. In our experiments, however, we found that this vapor pressure is not sufficient for the growth of nanowires/nanorods. Hence we have to increase the temperature to find substantial amount of Zn in vapor form. In other words, the optimal amount of Zn vapor for the growth of nanowires/nanorods is obtained from the liquid phase in which case the expression for vapor pressure of Zn is given by equation (7). Fig. 3-3 shows the vapor pressure of liquid Zn, from equation (7), as a function of temperature. It increases exponentially with temperature. The inset in Fig. 3-3 shows the vapor pressure and temperature regions (~80 mm Hg and ~993 K) where nanowires/nanorods have been grown.

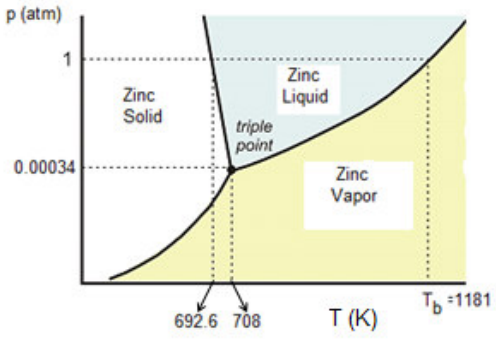

Fig. 3-2. Phase diagram of Zn.

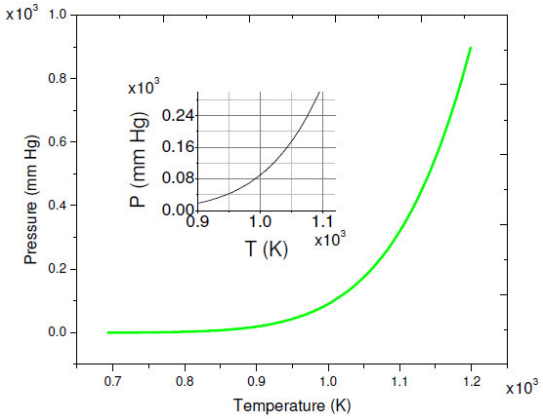

Fig. 3-3. Vapor pressure of liquid Zn.

3.3. Growth Mechanisms

Understanding the growth mechanisms of nanostructures is crucial to have a better control over the desired products. Hence, in the next sections a brief review of the most commonly proposed mechanisms for the growth of 1D nanostructures will be presented, followed by the proposed nucleation and growth, the two fundamental stages for the growth of a crystal from a solid, vapor or liquid state, for the nanowires/nanorods. Among the different growth mechanisms such as Vapor-Liquid-Solid (VLS), Vapor-Solid (VS), and Solution-Liquid-Solid (SLS), VLS and VS growth mechanisms are the most common vapor transport processes proposed to the growth of 1D ZnO nanostructures synthesised by thermal evaporation technique [49-52].

3.4. VLS Mechanism

The concept of VLS was first introduced by R. S Wagner and W. C Ellis from their detailed studies of the morphology and growth of Si whiskers [51]. Subsequent studies have reported the growth of 1D nanostructures with the VLS mechanism. The VLS mechanism is mostly characterised by the presence of nanoparticles caped at the end of 1D nanostructures and usually a metal catalyst is used during the growth. The metal catalyst and the appropriate synthesis temperature are chosen from the equilibrium phase diagram in order that the catalyst forms a liquid alloy with the material which is intended to form 1D nanostructure, for instance, gold (Au) and germanium (Ge) in Fig. 3-4B.

The liquid catalyst alloy cluster serves as a preferential site for absorption of the reactant and, when it is supersaturated, as a nucleation site or seed for crystallization. The growth of 1D nonostructures (e.g., nanowires/nanorods) is directed by the catalyst droplet and the diameter of the wires/rods is determined by the size of the droplet. The growth of nanowires/nonorods, however, occurs preferentially in the presence of the reactant as long as the catalyst remains liquid. When the temperature is below the eutectic temperature of the catalyst alloy or the reactant is no longer available the growth terminates and finally the catalyst will remain at the tip of the nanowires (Fig. 3-4A).
Recently, ZnO nanowires have been grown on different substrates using metal catalysts such Au, copper (Cu), and tin (Sn) to assist and control the growth process. C.Y. Lee et al.

[52] have synthesised single crystalline ZnO nanowires grown on Si(100) substrates by VLS mechanism from ZnO and graphite powders in a temperature range of 850-950 °C and inert atmosphere. According to this work, there are at least four different stages involved in the VLS mechanism for growth of ZnO nanowires, (i) Au film deposition, (ii) alloy nanoparticles formation, (iii) absorption and nucleation and (iv) epitaxial growth of ZnO nanowires.

The 1D nanostructures grown by VLS mechanisim are usually well aligned and uniform in diameter and length. However, the need for selection of appropriate catalyst and the difficulty to remove it from the final products are its main limitations.

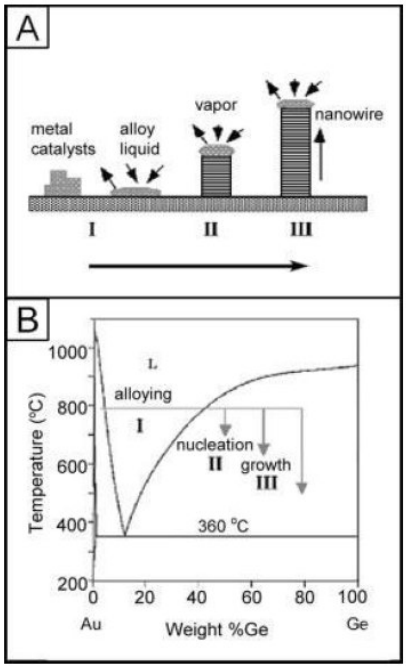

Fig. 3-4. A) Schematic illustration showing the growth of a nanowire via the Vapor-liquid-solid (VLS) mechanism. B) The binary phase diagram between Au and Ge, with an indication of the compositional zones responsible for alloying, nucleation, and growth [49].

3.5. VS Mechanism

VS mechanism was first proposed and theoretically modelled by Burton, Cabrera, and Frank and later elaborated by Sears ([53] and references therein). This growth mechanism is also characterised by vapor species generated by evaporation, chemical reduction or other kinds of gas reactions. The vapor species are subsequently transported by the help of the temperature gradient and/or a carrier gas and condense onto substrates placed in the lower temperature regions. Unlike VLS, here no metal catalyst is used and it has been

demonstrated that with proper control over the supersaturation level, the VS mechanism is capable of producing rich varieties of 1D nanostructures such as nanowires, nanoneedles, nanobelts and nanorods in moderately large quantities [49].

Many research groups have proposed VS mechanism to explain the growth of 1D ZnO nanostructures. For example, G. Shen et al. [54] have proposed the VS mechanism for the growth of vertically aligned ZnO nanonails and nanopencils fabricated by thermal evaporation process. In this process it has been proposed that first Zn evaporated and then oxidised by the oxygen in the reaction system to form ZnO_x gases. The newly formed ZnO_x gases were transported and deposited on Si substrate in the low temperature region to form a thin layer of ZnO film at an early stage. Second, further evaporation, oxidization, and nucleation caused homogeneous epitaxial growth of small ZnO nanorods from the ZnO film. With continuous deposition and growth, 1D ZnO nanostructures in the [0001] preferred growth direction were finally obtained. Similarly A. Umar and co-workers [55] have reported a VS growth mechanism for the synthesis of ZnO nanostructures on Si substrate by the thermal evaporation of high purity metallic Zn powder in the presence of oxygen without using any catalyst or additive. In this study no metal particles or other impurities were detected in the growth front of the obtained products as confirmed from field emission scanning electron microscopy (FESEM) and transmission electron microscopy (TEM) observations of the as-grown 1D ZnO nanostructures and then the authors have concluded VS mechanism for the growth of the nanostructures. X. Zhang et al. [50] have also suggested the VS mechanism for the growth of well aligned ZnO nanowires synthesised by thermal evaporation method using c-oriented ZnO thin films as a substrate without any catalyst or additive. According to this study, temperature provides energy for Zn particles to be vaporised, transported along the carrier gas flow and oxidised. Since the thin films are oriented along the [0001] direction which is the preferential growth direction of ZnO nanowires and the lattice constant of the substrate and the nanowires are exactly the same, the ZnO nanowires could continue to grow along the [0001] direction easily soon after Zn particles deposited on the substrate.

Compared to the VLS, VS mechanism is very dependent on the type of the substrates used and the thermodynamic conditions during the growth, since there is no alloy droplet which guides the growth of 1D nanostructures. Here, the incoming vapor is captured by cracks,

grains and grain boundaries, sprinkled particles or any defect on the substrate. However, the capturing efficiency of the defects is not as effective as the alloy droplets in directing the growth of 1D nanostructures [53]. Therefore, to facilitate the growth in a directed and well aligned ways, substrates which have close lattice match (or similar crystal orientation) with the material to be grown are often used for the growth of 1D nanostructures. In our case, Zn particles were sprinkled on the surfaces of Si and Al_2O_3 substrates to assist the capturing of the incoming vapor and formation of ZnO at the early stage. Then, as discussed in section 1.2.1, ZnO will under go various surface reconstructions and self-organized growth of different nanostructures, depending on the nucleation and growth kinetics which will be discussed in the next section. The main limitation of VS growth mechanism is lack of controlling the geometry, alignment and precise location of the nanostructures. Consequently, 1D nanostructures grown with VS mechanism usually have arbitrary orientation, non-uniform distributions and mixed morphologies. Its major advantage over the VLS mechanism is that no metal catalyst is used and hence unintentional introduction of foreign impurities into the nanostructures will be minimized.

3.6. Nucleation and Growth of Nanowires/Nanorods

The fact that there was no any metal catalyst used during the synthesis of the nanowires/nanorods, coupled with the information in the above discussions about the characteristics of the two growth mechanisms will lead us to suggest that the growth of nanowires/nanorods in this work best fits the VS mechanism. Hence, it can be explained that Zn vapor is transported and condensed onto the substrate surfaces and/or sprinkled Zn particles. The sprinkled Zn particles, grains and grain boundaries would act as trapping sites for the incoming Zn vapor. Furthermore, since the substrate temperature is relatively lower than that of the source, the sprinkled Zn particle might be in the form of liquid droplet which could have better capturing capacity for Zn vapor in the early stage. Here, ZnO vapor can also be transported to the lower temperature regions but with fewer amounts than that of Zn vapor because of the following reasons: first, the vapor density of ZnO is obviously larger than that of Zn. Hence, compared to the Zn vapor, it will not be easily transported longer distances down to the substrate regions by the carrier gas and the temperature gradient. Second, under non-equilibrium conditions the formation of stable ZnO vapor will be less probable. Even if there is ZnO vapor, much of it will deposit on the

surface of the source and only on the substrates placed close to the source. On the other hand, Zn vapor will be relatively easy to be transported to the substrate regions and react with oxygen to form ZnO, under favourable conditions for the growth of the observed nanostructures. Once ZnO is formed, the growth of the nanostructures, including ZnO seeds which in turn serve as nucleation sites for further growth of 1D nanostructures, will proceed in a self catalysing manner. The XRD results indicate that one of the preferred directions of the seeds/nanostructures is along the c-direction (Fig. 4-8). Moreover, as it can be confirmed from the SEM images in section 4.2.1, the nanowires and nanorods grew on the surfaces of bulk seeds. As a result, it can be proposed that the growth of nano-sized wires and rods has started from the surfaces of these seeds after an initial nucleus of radius r is created on their surfaces. In this case the free energy change for making a unit volume of solid is given by [56]

$$\Delta G = -V\Delta G_v + A\gamma_{sv} \qquad (8)$$

where V is the volume of nucleus formed, A is the area of the nucleus with extra surface free energy γ_{sv} per unit area created, and ΔG_v the change in Gibb's free energy per unit volume of the solid phase.

For nanowires and/or nanorods, the growth nucleus can be assumed to be very small in which case the free energy change in creating a nucleus as a pill box shape of height l and radius r (a small nanorod) can be written as [56]

$$\Delta G = -\pi r^2 l\Delta G_v + 2\pi r l\gamma_{sv} \qquad (9)$$

The Gibbs free energy per unit volume is dependent on supersaturation level, S, of the vapor and is given by

$$\Delta G_v = \frac{kT}{\Omega}\ln(\frac{P_v}{P_s}) = \frac{kT}{\Omega}\ln(1+S) \qquad (10)$$

where the degree of supersaturation is defined by

$$S = \frac{P_v - P_s}{P_s} \qquad (11)$$

where P_s is the saturated vapor pressure at equilibrium for a particular temperature and P_v is the actual pressure in gas phase. Thus, if the supersaturation level equals zero then the surface energy term dominates and there will be no nucleation at all. On the other hand if $S > 0$ the nucleation occurs spontaneously. In the case of nanostructure growth, the value of S is much larger than unity [53]. The graphical representation of the free energy change

described by equation (9) can also be seen schematically as in Fig. 3-5. From this figure one can easily see that the newly formed nucleus is stable only when its radius exceeds a critical size *r**. A nucleus smaller than *r** will disintegrate back in to the vapor form to reduce the over all free energy, whereas a nucleus larger than *r** is stable and continues to grow bigger and bigger [57].

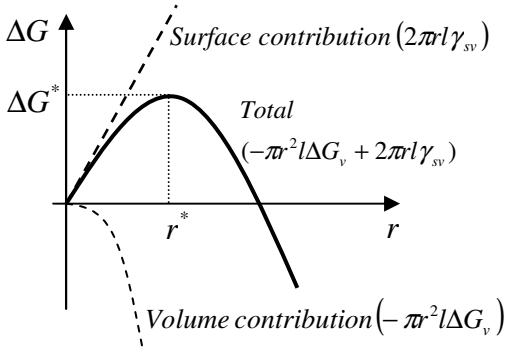

Fig. 3-5. Schematic representation of total Gibbs free energy as a function of nucleus radius.

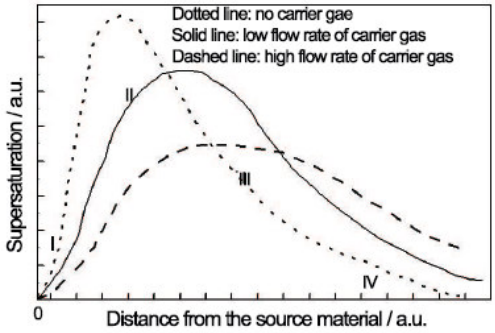

Fig. 3-6. Supersaturation profile of ZnO vapor in the reactor under different flow rate of carrier gas along the distance downstream from the source material, ref(115) in [53].

The critical radius for the formation of the nucleus can be determined from equation (9) by equating the slope of ΔG to zero at the critical radius, *r** (Fig. 3-5). Then the critical radius will be $r^* = \frac{\gamma_{sv}}{\Delta G_v}$. The Gibbs free energy at the critical radius can also be written as

$$\Delta G^* = \frac{\Omega \pi l \gamma_{sv}^2}{kT \ln(1+S)} \qquad (12)$$

This critical free energy change can be regarded as the energy barrier that a nucleation process must over come to proceed to the growth step.

And the rate of nucleation for the formation of the growth nuclei is given by [53,56]

$$\frac{dN}{dt} = B \exp\left(\frac{-\Delta G^*}{kT}\right) \qquad (13)$$

where *B* is a constant which is proportional to the number of atoms incident on the surface. This equation indicates that high supersatuartion results in law critical energy (barrier) which favours the formation of large number of nuclei. A typical diagram of supersaturation profile in a reactor under different flow rates of the carrier gas is represented in Fig. 3-6. The effect of supersaturation and temperature on the nanowires/nanorods will be discussed in section 4.2.1.

Chapter 4:

4. Experimental Description and Characterisations

4.1. Experimental Description

In the experiment, Zn powder (99% purity), Si and Al_2O_3 substrates, O_2 and N_2 gases were used. Zn and O_2 were used as a source whereas N_2 was used to create an inert atmosphere and help transport the vapor down the stream along the gradient of temperature.

The schematic diagram of the experimental setup is presented in Fig. 4-1. Here, unlike several literatures have reported, there is no need of using an alumina boat for the synthesis of nanowires/nanostructures. Instead, a long flat alumina plate of length 20 cm and width 2.3 cm was used. The powder was loaded on another flat alumina plate with dimension about 5.0 cm length and 2.0 cm width and then it was placed on the top of the long alumina plate. This was for the purpose of putting the source material at a level which at least equals the surface of the substrates so that the vapor will not encounter a barrier while it is going down to the substrates. The source material (powder) covered an area of about 4.5x2 cm. Small pieces of substrates (Al_2O_3 or Si) with dimensions about 1-2.5 cm in length and 1-1.5 cm in width were placed next to the source material and arranged in queue on the longer plate down the stream of temperature gradient (I, II, II and IV in Fig. 4-2). To create high temperature gradient along the alumina tube, the right side of the tube end was pulled out 11.0 cm and then the tube had a total length of 29.5 cm from the centre of the furnace. After the furnace temperature reached and stabilized at the desired temperature value, temperature data were recorded using the thermocouples and then the source material was placed in the alumina tube, with its left end located at the centre of the furnace. The left and the right ends of the alumina tube were closed with steel caps and sealed with plaster. Then O_2 and N_2 gases were released from their respective sources to enter via the left end of the tube and leave out through the right one. The desired furnace temperature was kept constant during the synthesis time. During this time, the source material mainly evaporated, transported and deposited on the substrates. After the synthesis time, the furnace was turned off and cooled down to room temperature while O_2 and N_2 were flowing through the whole cooling process. To obtain the optimal synthesis parameters, a number of

experiments were conducted by varying temperature, source materials, substrates, O_2 and N_2 gas flow rates. Fig. 4-2 shows the temperature profile along the alumina tube when the furnace temperature was set at 720 ºC.

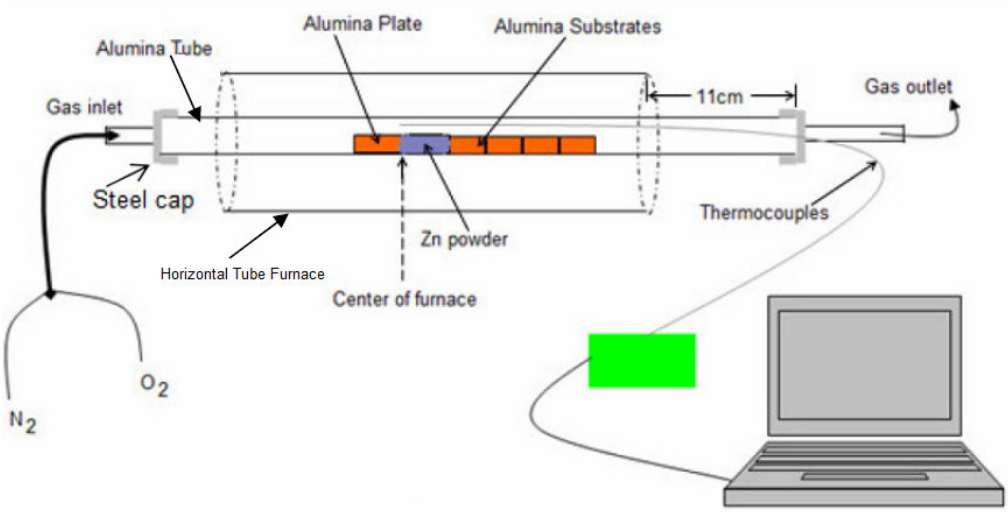

Fig. 4-1. Schematic diagram of the experimental setup for the synthesis of ZnO nanostructures.

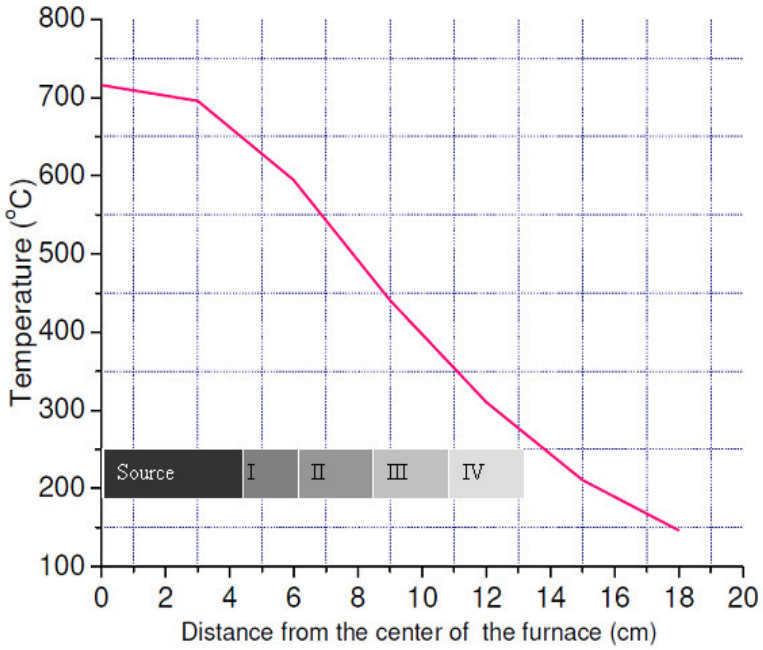

Fig. 4-2. Temperature profile in the alumina tube at furnace temperature of 720 ºC. I, II, III, and IV denote Substrate-I, Substrate-II, Substrate-III, and Substrate-IV, respectively.

4.2. Characterisations

Using scanning electron microscopy, SEM (ZEISS-1540XB), detailed explanations about the morphology of the as-grown nanostructures and effects of the processing parameters on the structures have been reported in the project part of this work. In the following sections, the SEM, X-ray diffraction (XRD), and Photoluminescence of the four samples, nanowires and nanorods, will be presented. The four samples were obtained from four different experiments, the first four experiments in Table-2. In all four experiments, the temperature of the furnace and the synthesis time were 720 ºC and 80 minutes, respectively. The temperature profile in the alumina tube is shown in Fig. 4-2. In each experiment number of substrates sprinkled with Zn particles and denoted as Substrate-I, Substrate-II, Substrate-III, Substrate-IV were placed on the flat alumina plate in order, down the stream of the temperature gradient. From this graph, the range of distances and the temperature at which one can find the optimal product could be clearly known. Accordingly, the powder (source), Substrate-I, Substrate-II, Substrate-III, and Substrate-IV cover distances of 0.0-4.5 cm, 4.5-6.2 cm, 6.2-8.4 cm, 8.4-10.9 cm and 10.9-12.6 cm, respectively, the centre of the furnace being the reference point. Whereas the corresponding temperature ranges were 715-645 ºC, 645-585 ºC, 585-470 ºC, 470-358 ºC and 358-290 ºC, respectively. Hence, the SEM images of the as-grown nanowires/nanorods on each substrate could be explained in terms of the parameters such as distance from the source, substrate temperature and flow rates of gases (O_2 and N_2). All the images of the nanorods were taken by SEM (SU-70) whereas for the nanowires SEM (ZEISS-1540XB) was used.

4.2.1. SEM Images of Nanowires/Nanorods

Fig. 4-3 shows the SEM images of nanorods grown on Si substrate, Substrate-I, with O_2 and N_2 flow rates 80 and 450 sccm (standard cubic centimetre per minute), respectively. Most parts of the substrate area can be seen being clean, without having ZnO seeds or layers. However, in some areas of the substrate surface few seeds have nucleated and grown. As it can be seen from the magnified image in Fig. 4-3b, the nanorods grow on the surface of seeds indicating that the self catalysing process had played the role for the nucleation and growth of the nanorods (section 3.5 and 3.6). In other words, the substrate

does not have a direct effect on the nucleation and growth of the rods. The rods have an average length and diameter of 1.62 μm and 120 nm, respectively.

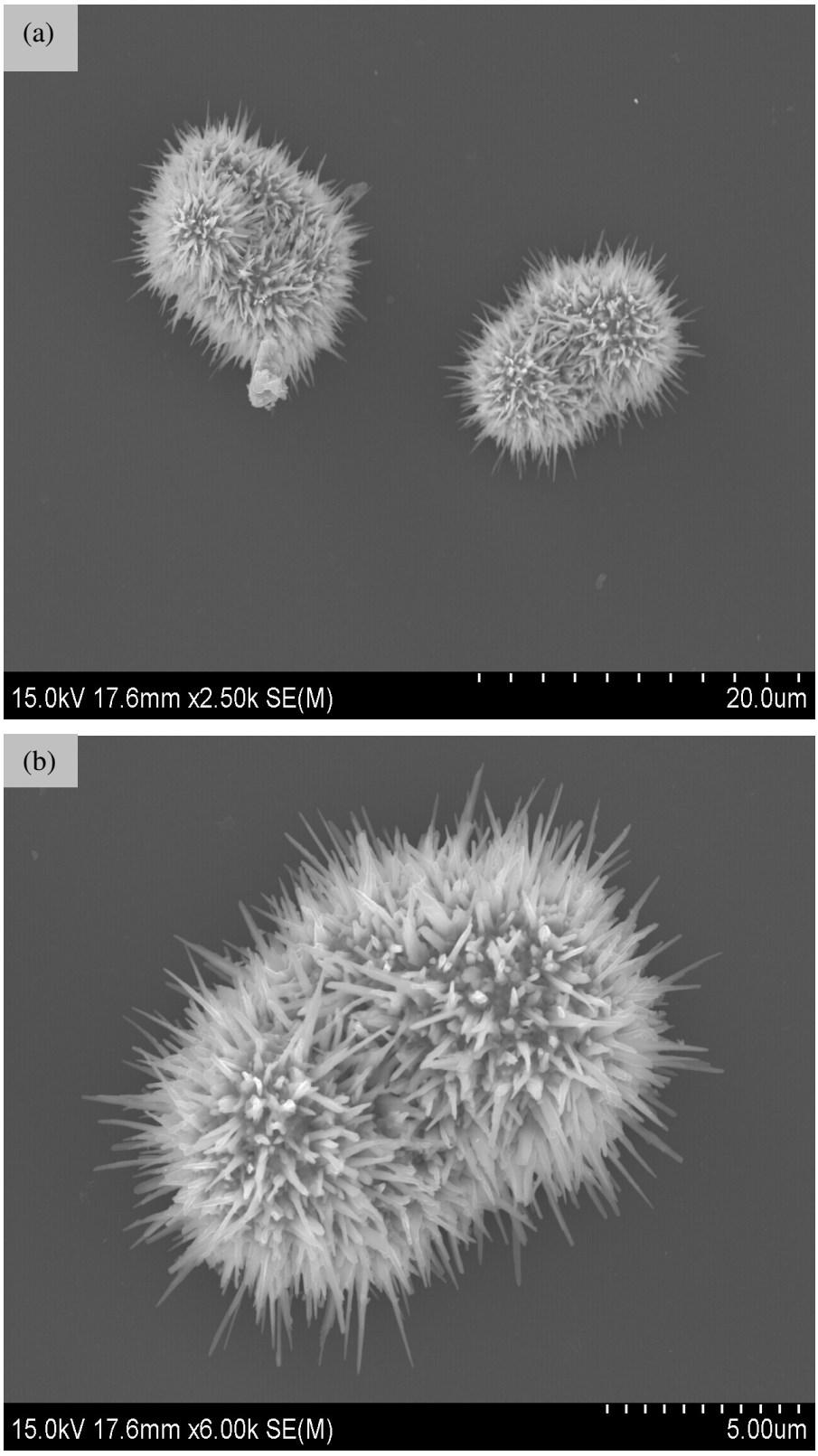

Fig. 4-3. (a) SEM images of the nanorods grown on Si substrate, Substrate-I, (b) magnified image.

Changing the O_2 flow rate to 100 sccm, a change on the morphology of the nanostructures has been observed as in Fig. 4-4. Here, the optimal products were obtained in Substrate-II. In this case, the major part of the substrate area is covered with ZnO layer. This is due to the fact that more oxygen was flowing in the tube and there would be relatively high rate of ZnO formation leading to films or layers that cover the substrate surface. However, like that of Substrate-I, here few seeds have grown on the substrate and the nanowires grow on the surface of the seeds. The magnified image in Fig. 4-4b shows the diameter of each nanowire varies over its length. Typical wire of length 7.15 μm with bottom and top diameters 192 and 43 nm, respectively, have been grown on this substrate. One factor for such variation in diameter could be attributed to the local supersaturation of the vapor. Under higher supersturation level, the nanostructures formed will be layer of ZnO or bulk ZnO due to the high nucleation rate and competition for capturing of the incoming vapor. In this case, formation of bulk ZnO will occur throughout the entire synthesis time. In other words, the nucleation and growth of the nanowires/nanorods will not start in the early stages until the optimal supersaturation is attained. Accordingly, it seams that the growth of the nanowires on this substrate started late (may be at the end of the synthesis time) and after the furnace was turned off. During the cooling process the diameter of the nanowires could decrease, following the gradual decrease of Zn vapor, and finally the growth would end after some critical temperature. If the flow of oxygen had been stopped during the cooling, the growth of the nanowires would have terminated, leaving the nanowires being shorter in length and relatively uniform in diameter.

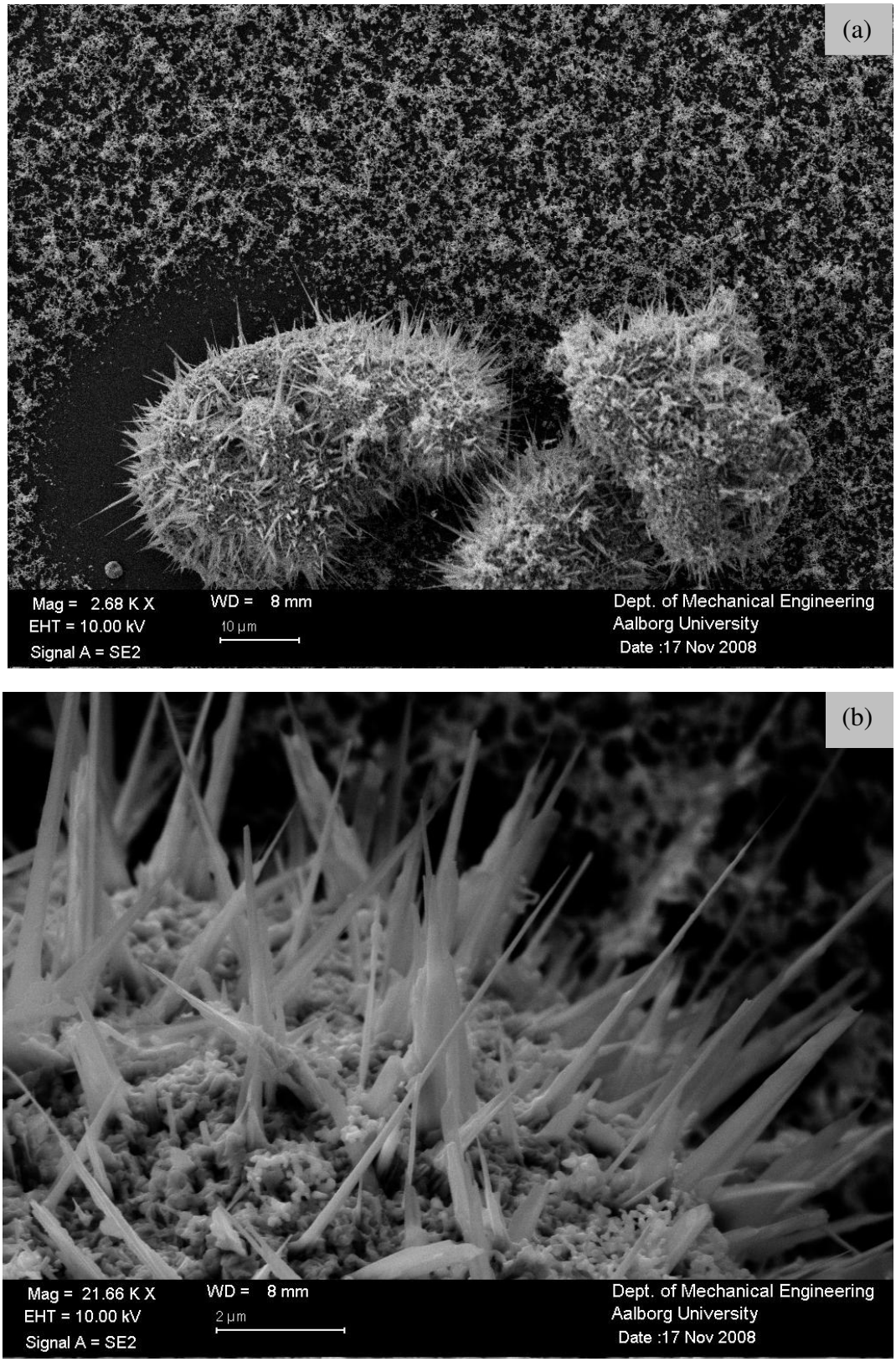

Fig. 4-4. (a) SEM images of the nanowires grown on Si substrate, Substrate-II, (b) magnified image.

In other experiments, long nanowires with uniform diameter have been grown on Al_2O_3 substrates. As in the case of nanowires/nanorods on Si substrates, here the nanowires have also started nucleation and growth from the surfaces of seeds which might use the sprinkled Zn particles, grains or grain boundaries as their nucleation sites.

Fig. 4-5 presents the nanowires grown on Al_2O_3 substrate, Substrate-I, with O_2 and N_2 flow rates 100 and 350 sccm, respectively. As it can be seen, the surface of the substrate is very clean and nanowires of very high density grow on the surface of spherical seeds. The diameters and lengths of the nanowires vary from 40 to 160 nm and 3 to 6 µm, respectively. Fig. 4-3 and Fig. 4-5 reveal that the nanostructures on Si and Al_2O_3 substrates of Substrate-I have very similar features. In both cases the substrate surfaces are very clean of ZnO layer, the seeds have spherical shape, and the nanowires/nanorods are very dense and shorter than the corresponding nanowires grown on Substrate-II. Such similarities might be due to the substrate temperature and the vapor pressure which are almost the same on Substrate-I.

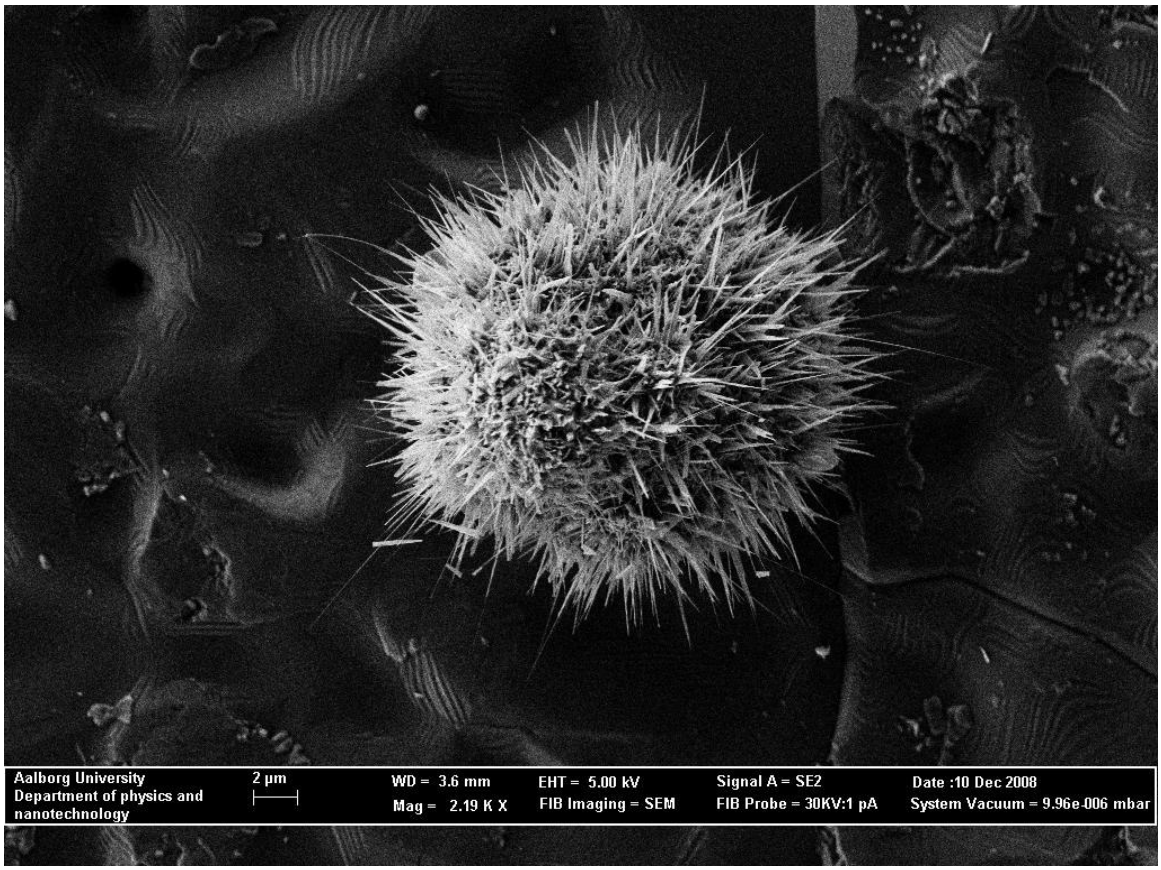

Fig. 4-5. SEM images of the nanowires grown on Al_2O_3 substrate, Substrate-I.

On the other hand, the nanowires in Fig. 4-6 are obtained from Substrate-II with flow rates of O_2 and N_2 100 and 450 sccm, respectively. The Al_2O_3 surface consists of bulk ZnO layer, seeds without wires, and seeds with high density nanowires. Unlike the corresponding nanowires on Si substrate (Substrate-II), here nanowires are long and relatively uniform in diameter. Wires of typical length 22.63 μm and diameter 77.7 nm have been grown on this substrate.

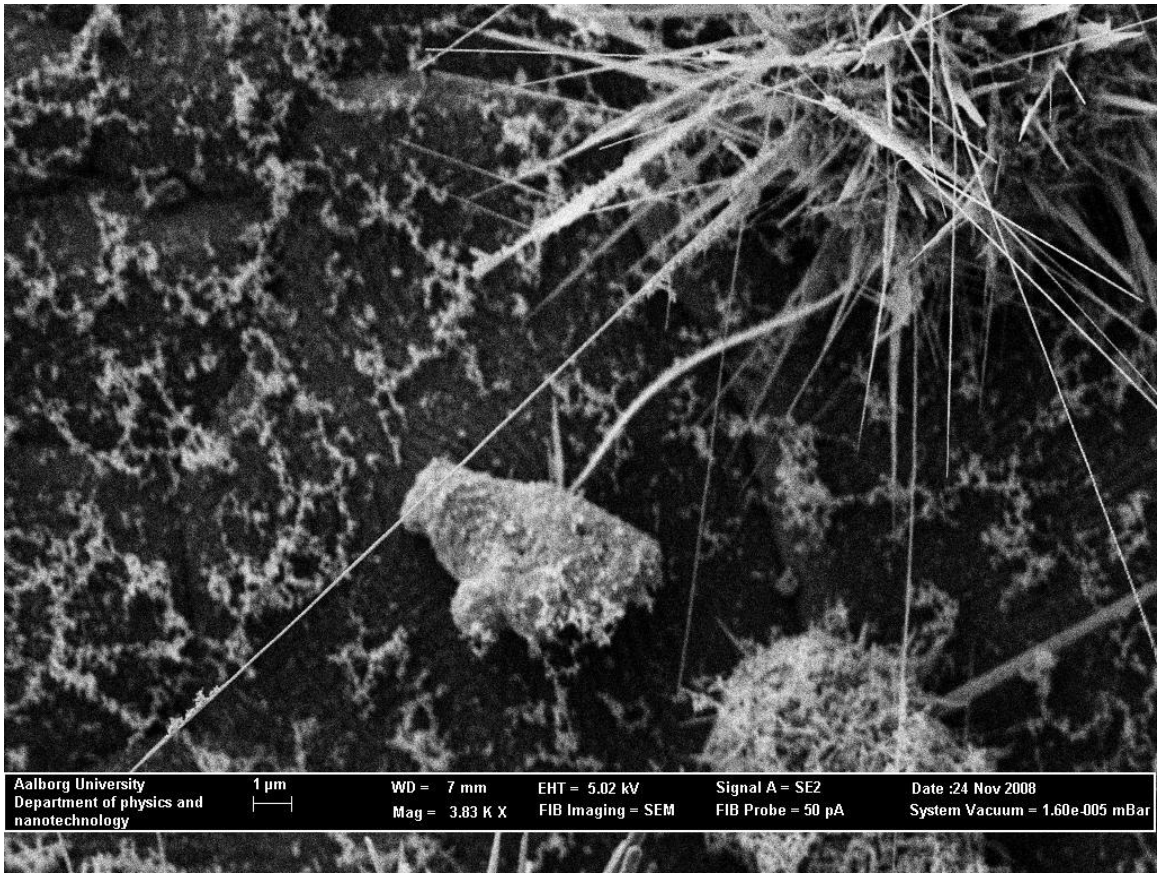

Fig. 4-6. SEM images of the nanowires grown on Al_2O_3 substrate, Substrate-II.

The morphology of the grown structures can be attributed to various factors such as supersaturation, substrate temperature, and substrate type. The supersaturation profile of the vapor from the source down to the substrates can be understood from Fig. 3-6. In general supersaturation level decreases as one goes away from the source where the maximum temperature is obtained. The optimal supersaturation reaching the substrates depends on the source temperature and distance from the source. From equation (12) the

larger the supersaturation is the smaller the critical Gibbs free energy of formation which leads to the formation of large number of nuclei in short period of time (high rate of nucleation equation (13)), leading for the formation of films, bulks and undefined morphologies of ZnO. Besides the supersaturation, substrate temperature which depends on distance from the source has also a prominent effect on the rate of nucleation; the higher the temperature is the higher the nucleation rate. Hence, the rate of nucleation affects the morphology of the nanostructures. It has been also reported that the high rate of nucleation and growth could also result in the formation of excessive native defects in the nanostructures, especially when the ratio of oxygen and Zn in the vapor phase is imbalanced [32]. The type of the substrate is also another factor for growth of various nanostructures. For instance, good lattice matching between the substrate and the nanostructures is preferable to avoid strain effects and have good crystal quality [58,59]. On the other hand, cracks or defects on the substrates can also act as effective collecting sites for incoming vapor particles, where nucleation and growth of seeds proceed preferably [53]. This would be the most probable case for the observed nanostructures in this work because the seeds were seen to grow first on the substrate surfaces, for example on the grains of the substrate as it can be seen in Fig. 4-7a. Then the nanowires and nanorods grew from the surface of these seeds, suggesting that the growth of nanowires/nanorods was indirectly influenced by the substrate type. The differences between the morphologies of the nanowires on Si (Fig. 4-4) and Al_2O_3 (Fig. 4-6) substrates is attributed only to the effect of substrate type. The observation of long and relatively uniform diameter of nanowires on Al_2O_3 substrate indicates that most of the growth process of nanowires occurred during the synthesis time in which Zn vapor was sufficiently available. This can be confirmed from the sizes of the seeds on which the nanowires were grown. The average size of the seeds grown on Al_2O_3 substrate (Fig. 4-6) is about 10 µm whereas that of the seeds grown on Si substrate (Fig. 4-4) is about 36 µm. This implies that the growth of seeds on Al_2O_3 substrate was terminated in the early stages of the synthesis time and then the nucleation and growth of nanowires could start soon on this seed, resulting in long and uniform diameter nanowires. To the contrary, the growth of seeds on Si substrate could take place almost till the end of the synthesis time because the seeds are bigger on this substrate (Fig. 4-4), supporting the previous discussion that nucleation and growth of the nanowires started very late.

The flow rate of gases is the other parameter which significantly changes the morphology of the resulting nanostructures at a particular distance from the source. The higher the flow rate of the carrier gases, the longer does the vapor particles transport before depositing on the substrates. If there is no carrier gas, most of Zn vapor particles as well as ZnO will be deposited on the surfaces of the source material, resulting in impeding Zn vapor generation and termination of nucleation and growth of nanostructures on the substrates. On the other hand, for extremely high flow rate, the vapor particles will be swept out of the alumina tube by the carrier gas. If we consider the nanowires grown on Al_2O_3 substrates, the effects of flow rate of the carrier gas on the nanowires/nanorods could be easily understood. As mentioned before only the flow rate of N_2 was different for the two substrates. In Substrate-I, N_2 flow rate was 350 sccm. As seen in Fig. 4-5, the Al_2O_3 surface is clean and the seeds were nucleated and grown from either the surface of Al_2O_3 or the sprinkled Zn particles. The nanowires which look like a well combed hair were grown from the surfaces of spherical seeds, highly dense and erected straight outwards. However, as one moves away from the source, for example, to Substrate-II of the same experiment, the density of the nanowires on the seeds and their length decrease due to the low local supersaturation degree on this substrate (Fig. 4-7a). This effect is attributed to the low flow rate, 350 sccm, which does not carry as much vapor as the flow rate 450 sccm does. In other words, some of the vapor produced might be oxidised and deposited on the surface of the source while the remaining could be transported only to the substrates placed near to the source. Hence, the optimal position for the growth of nanowires in this experiment was found on Substrate-I which was closer to the source material. On the contrary, the nanostructures grown with N_2 flow rate of 450 sccm on Substrate-I of the other experiment (Fig. 4-7b) are different from the preceding results, as we can see from the images. Such differences clearly show the effect of gas flow rate on resulting structures. Since the 450 sccm is higher than the 350 sccm, large amount of vapor particles can be transported by the carrier gas to the substrate regions. Thus, deposition of the vapor on the source material is obviously less compared to the one which has the flow rate of 350 sccm. As a result, there could be a heavy drop of Zn vapor which resulted in the formation of thick layer of ZnO on the substrate surface, as seen in Fig. 4-7b. However, down the stream, the local supersaturation gets smaller and the formation of the thick ZnO layer on the surface of Al_2O_3 decreases (Fig. 4-6). Hence the optimal supersaturation for the growth of 1D

structure in this case is observed in the regions far from the source, Substrate-II (Fig. 4-6). The observed differences in the morphology of nanostructures on Si substrates (Fig. 4-3 and Fig. 4-4) can be explained in a similar way.

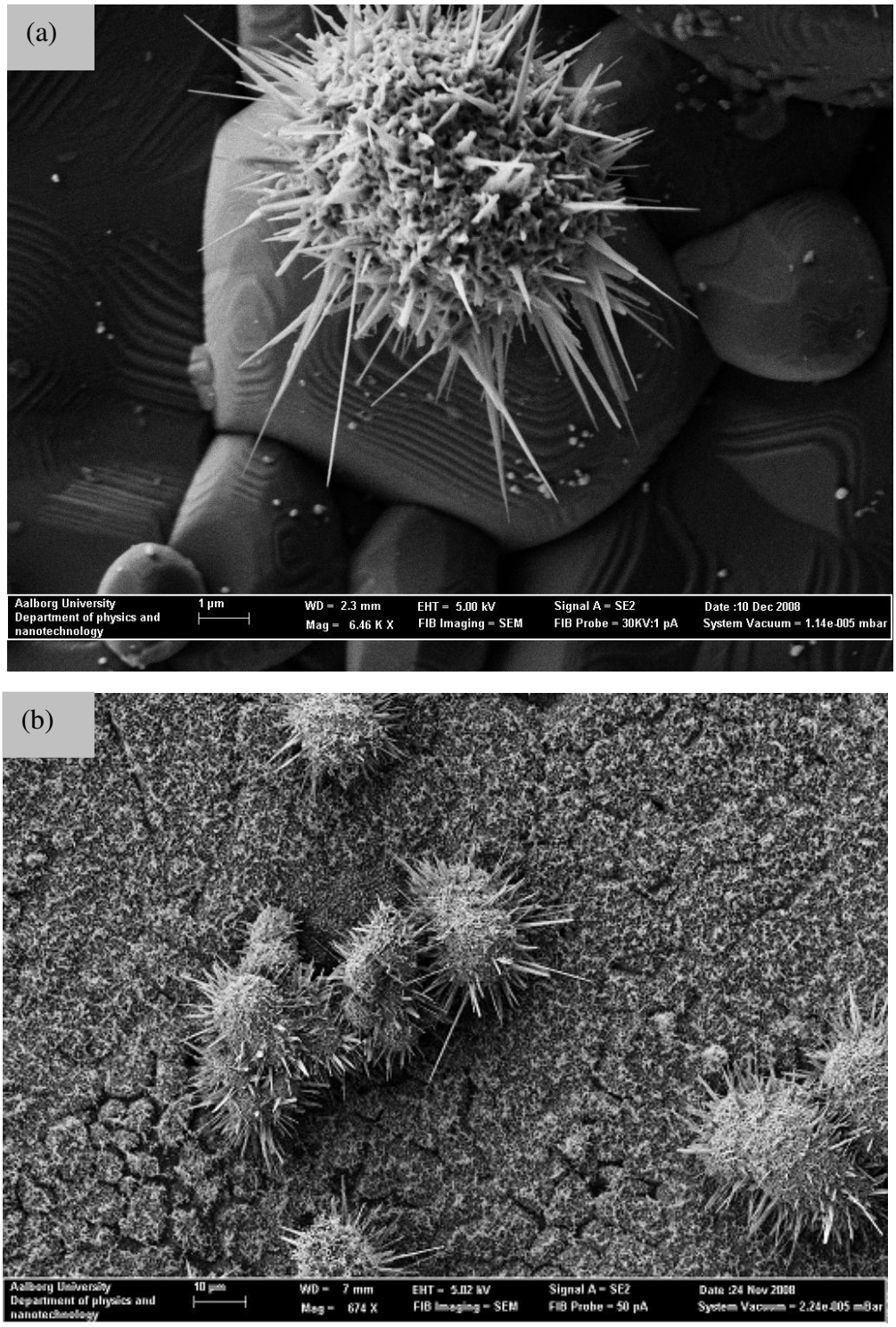

Fig. 4-7. SEM images of nanowires grown on Al_2O_3 substrates: (a) on Substrate-II with N_2 flow rate 350 sccm, (b) on Substrate-I with N_2 flow rate 450 sccm.

Table-2 Summary of the experimental results

No. Experiments	Furnace Temperature (ºC)	Type of source (powder)	Type of substrate	Synthesis Time (min.)	Gas flow rates (sccm)		Observed Structures
					O_2	N_2	
1	720	Zn	Si	80	80	450	• Nanorods Fig. 4-3
2	720	Zn	Si	80	100	450	• Nanowires and • Nanoneedles Fig. 4-4
3	720	Zn	Al_2O_3	80	100	350	• Nanowires Fig. 4-5
4	720	Zn	Al_2O_3	80	100	450	• Long nanowires • Short nanowires Fig. 4-6
5	650	Zn	Al_2O_3	90	100	450	• Nanowires and • Nanoneedls
6	720	Zn	Al_2O_3	80	100	350	• Nanowires
7	750	Zn	Al_2O_3	60	100	350	• Nanonedles • Short Nanowires
8	800	Zn	Al_2O_3	60	150	450	• nanotetrapods
9	690	Zn	Al_2O_3	90	87	300	• Few nanoneedles • Seeds without any nanostructure
10	700	Zn	Al_2O_3	80	100	450	• Nanowires and • Nanorods
11	850	ZnO + C	Al_2O_3	45	150	none	• Nothing observed
12	1150	ZnO + C	Al_2O_3	90	100	450	• Nanosheets • Nanorods

4.2.2. X-ray Diffraction of Nanowires/Nanorods

The crystal structure and orientations of the nanowires/nanorods were analysed using powder XRD (X'Pert MPD Philips X-ray diffractometer, CuK_α radiation of λ=1.5406 Å) operating at 40 kV and 50 mA.

Fig. 4-8 shows the XRD patterns of the nanowires and nanorods grown on Substrate-I and Substrate-II of Si and Al_2O_3 substrates (of Fig. 4-3, Fig. 4-4, Fig. 4-5 and Fig. 4-6). To identify easily peaks from the samples, the diffraction patterns of the substrates are also presented in the same figure (Fig. 4-8e and Fig. 4-8f). In general, the observed peaks of all the samples have very narrow bands with full width at half maxima (fwhm) $2\theta < 0.19^o$ and they are similar to the peaks indexed for the pure hexagonal wurtzite phase of bulk ZnO according to the standard JCPDS file No. 00-036-1451 with lattice parameters a=3.242 Å and c=5.188 Å. The most intensified peak in all the samples is along the orientation (101) followed by (100) and (002) orientations, implying that growth happened preferably along these directions. This is also similar with the referred JCPDS. The diffraction peaks from the Al_2O_3, Si and Zn are also indexed with JCPDS file No. 04-004-2852, 00-027-1402 and 00-004-0831, respectively. In this case Al_2O_3 is in the alpha phase, α -Al_2O_3.

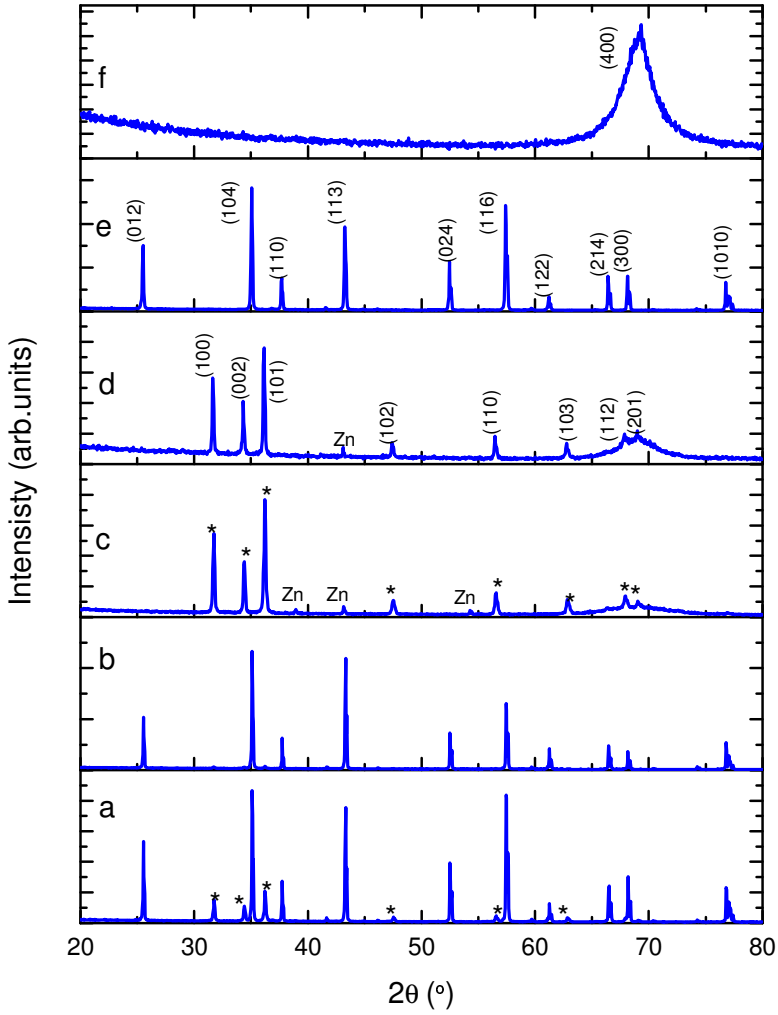

Fig. 4-8. XRD patterns of samples on Al_2O_3 and Si substrates and diffraction peaks of the substrates: a) nanowires on Al_2O_3 substrate (Substrate-II) grown with O_2 and N_2 flow rates 100 and 450 sccm, respectively, b) nanowires on Al_2O_3 substrate (Substrate-I) grown with O_2 and N_2 flow rates 100 and 350 sccm, respectively, c) nanorods on Si substrate (Substrate-I) grown with O_2 and N_2 flow rates 80 and 450 sccm, respectively, d) nanowires on Si substrate (Substrate-II) grown with O_2 and N_2 flow rate 100 and 450 sccm, respectively, e) Al_2O_3 substrate, f) Si substrate. The peaks marked by * are from ZnO.

Eight diffraction peaks from the samples can be seen on Si substrates (Fig. 4-8c and Fig. 4-8d). There are also additional peaks from the sprinkled or unreacted Zn that indicates the nanowires and nanorods on Si substrates have Zn impurities. Particularly, the nanorods grown with relatively low O_2 flow rate contain more residual Zn as it can be seen from the spectrum (Fig. 4-8d). On the other hand, the diffraction peaks of nanowires grown on Al_2O_3 substrates are highly dominated by the peaks from the substrate and only the most

intensified peaks of the samples can be unambiguously observed in the diffraction. Especially in the case of the nanowires grown on Al_2O_3 substrate with low N_2 flow rate, the diffraction peaks of the sample are almost negligible (Fig. 4-8b). This can be confirmed from the SEM images in Fig. 4-5 that the Al_2O_3 surfaces are barely covered by the ZnO nanowires or seeds and thus the X-ray beam might not access the sample. In general, diffraction from Zn impurities can not be seen on Al_2O_3 substrates though there are sprinkled Zn particles on these substrates as well. However, it might be dominated by the high intensity peaks from the substrates.

The prominent diffraction peaks of nanowires on the Al_2O_3 (Substrate-II, of Fig. 4-6) and nanorods on Si (Substrate-I, of Fig. 4-3) substrates are positioned at the same angles 31.73º, 34.42º and 36.22º, whereas the peaks from nanowires on Si substrate (Substrate-II, of Fig.4-4) are centered at 31.65º, 34.30º, and 36.14º. All the peak positions have been slightly shifted to lower angles compared to the corresponding standard peak positions 31.85º, 34.55º and 36.35º (JCPDS No. 00-036-1451). There are also slight deviations in the calculated lattice parameters. The lattice parameters, a and c, can be estimated using the theoretical formula

$$d_{hkl} = \frac{1}{\sqrt{\frac{4}{3a^2}\left(h^2 + k^2 + hk\right) + \frac{4}{c^2}}} \qquad (14)$$

where d_{hkl} is the interplaner spacing that can be obtained from Brag's law [64]

$$d_{hkl} = \frac{\lambda}{2\sin(\theta)} \qquad (15)$$

Therefore, using (15), for the nanowires on Si, the interplaner spacings are d_{100}=2.824 Å and d_{002}=2.611 Å for the planes (100) and (002), respectively. Substituting these values in equation (14) results a=3.261 Å, and c=5.222 Å. Similarly, for the nanorods on Si and nanowires on Al_2O_3 substrates the lattice parameters can be estimated to be a=3.253 Å and c=5.204 Å. Though these results show good agreement with the values reported in the previous literatures [21], such slight deviations are often attributed to the local strain around the impurities or lattice defects [58], indicating that the samples consist of considerable defects. The strain effects can be also resulted from lattice mismatch between the samples and substrates [59]. As it has been discussed in section 2.4 the defects can

have different origins such as vacancies of oxygen and Zn. Fig. 4-9 compares the intensity of the three major diffraction peaks of the samples on Al_2O_3 and Si substrates, for qualitative information. The relative intensity is highest for nanowires grown on Al_2O_3 (Fig. 4-8a) and the least for nanowires grown on Si substrate (Fig. 4-8d). In general, the XRD data suggest that the quality of the as-grown nanowires/nanorods depends on the growth conditions.

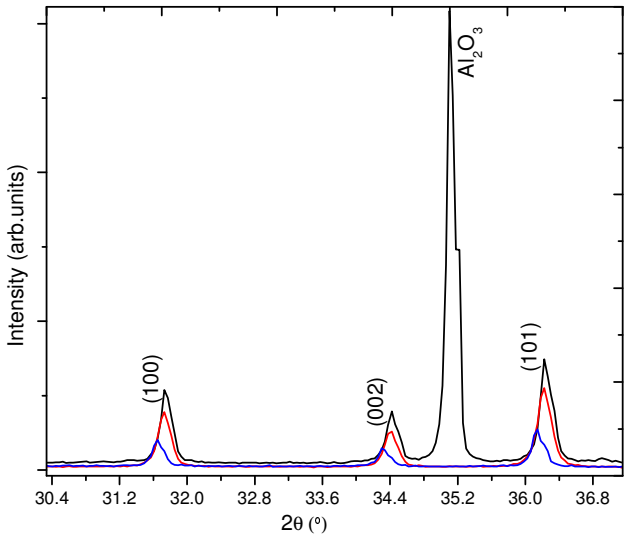

Fig. 4-9. XRD pattern showing relative intensity differences between peaks of the nanowires (blue color) on Si substrate grown with O_2 and N_2 flow rates 100 and 450 sccm, respectively, nanorods (red color) on Si substrate grown with O_2 and N_2 flow rates 80 and 450 sccm, respectively, and nanowires (black color) on Al_2O_3 substrate grown with O_2 and N_2 flow rates 100 and 450 sccm, respectively.

4.2.3. Photoluminescence Properties of Nanowires/Nanorods

Photoluminescence spectroscopy is very helpful technique in investigating the nature of defects which affect the material's quality and performance. In the case of wideband gap materials like ZnO having various intrinsic defects, the excitation spectra are very important to identify efficient excitation wavelengths (energies) at which the sample emits with its maximum intensity for a particular energy level. Because, besides the near-band edge absorption, the excitation spectra may contain multiple peaks corresponding to the absorption by several defect energy levels in the band gap. Hence, the luminescent property of the defects, the type of defects involved and fundamental transitions can be examined.

The room temperature and low temperature (12 K) emission and excitation spectra were measured using steady state photoluminescence. The 12 K measurement was performed by cooling the sample in a helium closed-cycle cryostat. The measurements were recorded using Fluorolog-3 model FL3-2T with a 450 W Xe-arc lamp as excitation source, double excitation spectrometer (TRIAX 320) fitted with a 1200 grooves/mm grating, a single emission spectrometer (TRIAX 320) fitted with a 1200 grooves/mm grating, a photomultiplier (R928) as a detector. The block diagram of the room temperature photoluminescence setup is depicted as in Fig. 4-10. To measure the excitation spectrum, the emission monochromator was fixed at a particular emission wavelength and then the intensity corresponding to the fixed wavelength was recorded at various excitation wavelengths. The emission spectrum was then measured by exciting the sample with a single wavelength which corresponds to one of the peaks in the excitation spectrum. In this case, the excitation monochromator was set at a particular wavelength while the emission monochromator scanned in a range of wavelengths. The excitation spectrum was monitored between 240 and 600 nm for the spectral distribution of the lamp and the emission spectrum was also adjusted for the spectral response of the monochromater and the detector.

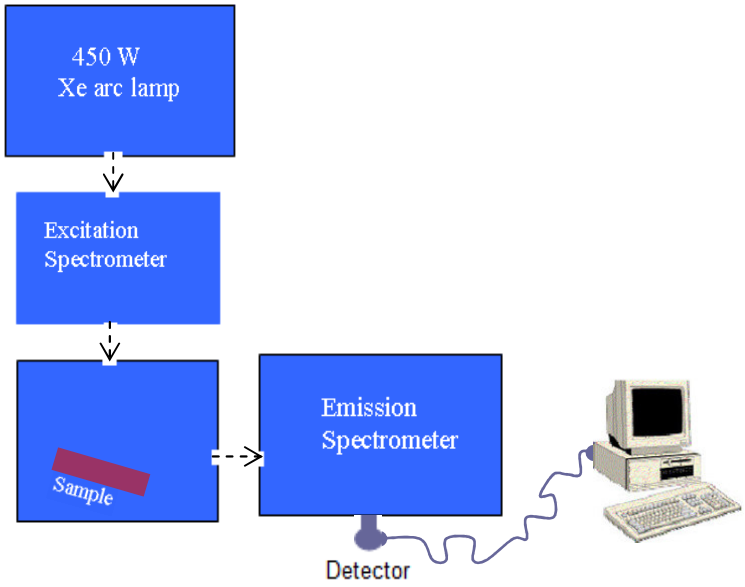

Fig. 4-10. Block diagram of the photoluminescence setup.

4.2.3.1. Photoluminescence spectra of Nanowires/Nanorods at Room Temperature

As it can be seen in Fig. 4-11, the room temperature excitation spectra of the nanorods and nanowires on Si substrates (Fig. 4-11a and Fig. 4-11b) and Al_2O_3 substrate (Fig. 4-11c) have almost similar profiles though they have some variation in the substrate temperature and amount of O_2 used during the synthesis. In all cases, wide excitation band in the range of 280 nm (4.43 eV) to 375 nm (3.31 eV) can be seen. Since this energy range is above the band gap energy of ZnO, in principle, it can excite the free electrons as well as excitons to the conduction band and higher energy levels. Based on the band gap energy, the transitions in the excitation spectra can be classified in two major bands attributed to the near-band edge (excitonic) transitions and defect related transitions within the band gap. In particular, the spectral regions to the higher energy (lower wavelength) side of the excitation spectra can be related to the transition of electrons and/or excitons to higher energy levels whereas the spectral regions to the lower energy (higher wavelength) side might be due to transitions to defect energy levels in the band gap. This can be confirmed from the corresponding emission spectra that there are only two emission bands, near-band edge emission, and defect related emission, for the entire excitation wavelengths used (Fig. 4-12).

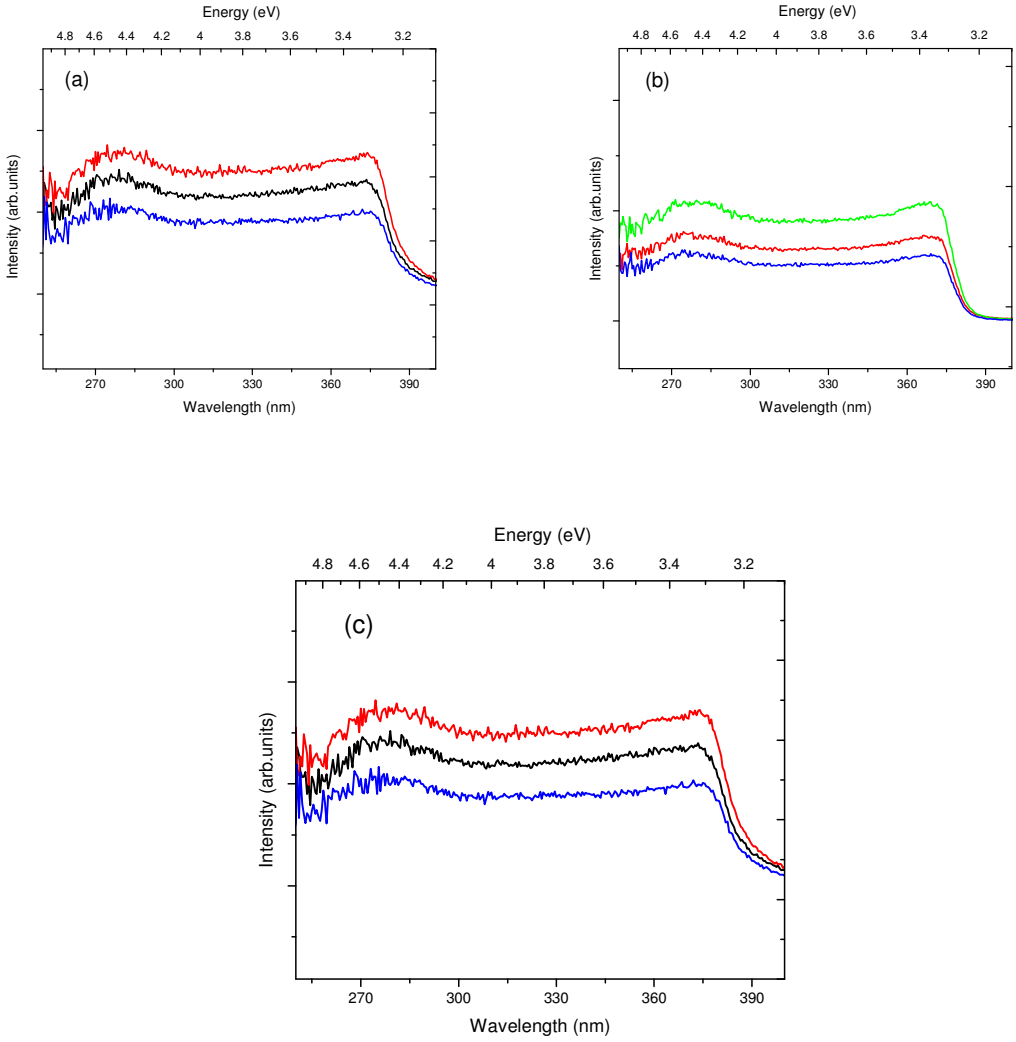

Fig. 4-11. Room temperature excitation spectra of the (a) nanorods on Si substrate, (b) nanowires on Si substrate and (c) nanowires on Al_2O_3 substrate, the emission wavelengths being monitored between 464 and 565 nm.

The emission spectra of the nanorods and nanowires on Si substrates consist of a dominant peak positioned at about 505 nm (2.45 eV) followed by a relatively weak peak at ~379 nm (3.27 eV) as in Fig. 4-12. There is no any significant change in the peak position of these bands with increasing excitation wavelength (decreasing excitation energy of photons). The two emission bands, in the visible and UV spectral regions, display a Gaussian profile. The emission spectra of the nanowires on Al_2O_3 substrates also exhibit these two emission bands (Fig. 4-13). However, the peak positions of the visible band and the UV band vary in the ranges of ~2.38–2.45 eV and ~3.21–3.26 eV, respectively, depending on the excitation

wavelengths used, suggesting that substrate type have effects on the emission spectra of the nanostructures.

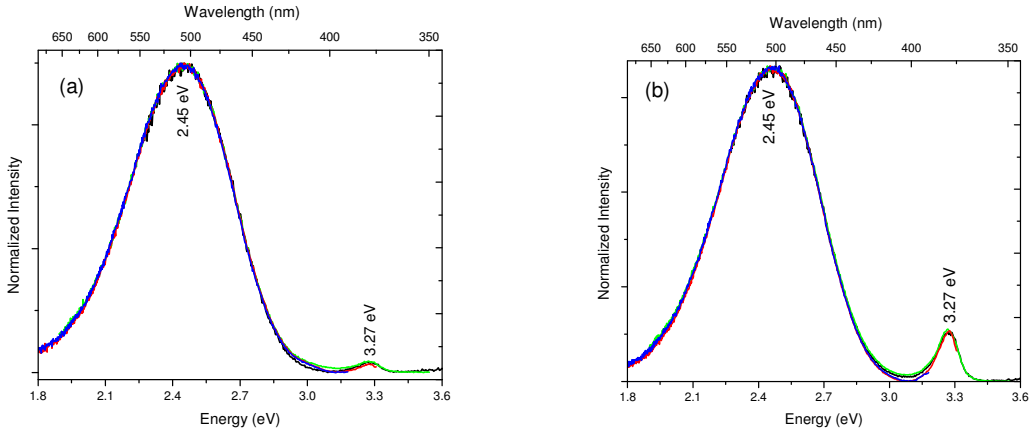

Fig. 4-12. Room temperature emission spectra of the (a) nanorods and (b) nanowires on Si substrate, excited at 280 nm (black color), 334 nm (green color), 360 nm (red color) and 375 nm (blue color).

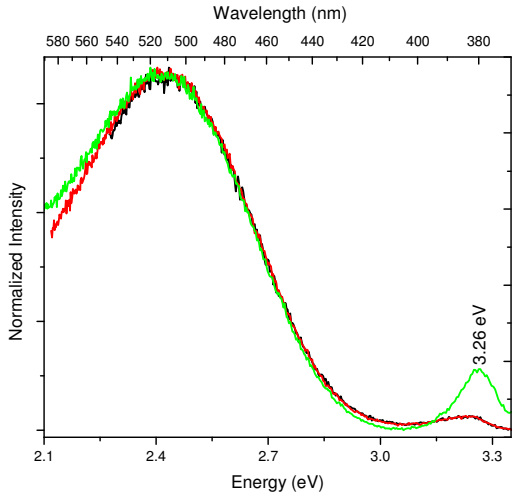

Fig. 4-13. Room temperature emission spectra of nanowires on Al_2O_3 substrate, excited at 280 nm (black color), 300 nm (red color) and 330 nm (green color).

The room temperature emission peaks in Fig. 4-12 and Fig. 4-13 can be ascribed to the defect related and excitonic transition lines, since their energies lie below and near to the band gap energy. The dominant emission band in the visible spectral region is often reported to be attributed to the intrinsic defects of ZnO despite there being some disputes on the origin of the defect associated with it, as discussed in section 2.4. The possible

chemical origin of the defects responsible for the green luminescence (GL) band in the emission spectra of nanowires/nonorods will be discussed later. On the other hand, the relatively narrow and weak UV band to the higher energy (lower wavelength) side in the emission spectra is commonly assigned to the near-band edge emission due to excitonic transitions [35,42,58]. As discussed in section 2.3, the electron-hole pairs, excitons, can be formed when the sample is excited with photon energy greater than its band gap energy. The consequent radiative recombination of these excitons will emit photon energy close to the band gap energy of the sample according to the conservation of energy in equation (2). Such emission is referred to as near-band edge emission or exciton emission. As seen from Fig. 4-12, for nanowires and nanorods on Si substrates, such emission band is positioned at ~3.27 eV. However, if the commonly accepted band gap energy, 3.37 eV, and exciton binding energy, 0.06 eV, of ZnO are considered at room temperature, the observed emission should have its peak position at 3.31 eV rather than at ~3.27 eV which is 0.04 eV below the expected free exciton transition line. Here, phonons may play the main role for such effect because the 0.04 eV is in the theoretically predicted energy spacing, 0.035-0.06 eV, between the A free exciton and its first longitudinal phonon replica ($FX_A^{n=1}-1LO$) transition lines at room temperature [39,61]. As reported in many literatures [21,27,39] the room temperature UV emission of ZnO samples is also attributed to phonon related emissions of the A and B excitons and their mixtures. For instance, the room temperature UV emission spectra of ZnO nanowires reported by A. Mohanta et al. [30] has a dominant peak at ~3.261 eV which was assigned as the first longitudinal phonon replica of the A free exciton recombination ($FX_A^{n=1}-1LO$) and the calculated energy separation between $FX_A^{n=1}$ and $FX_A^{n=1}-1LO$ is ~0.047 eV which accords well with the observed experimental result. In our case, the peak at ~3.27 eV could be tentatively assigned to phonon assisted transition of the A free exciton. However, temperature evolution of emission spectra should be considered to assign the peak more precisely. As discussed in section 2.2, lattice vibrations and thermal ionization of defects are promoted at high temperatures. In this case it is difficult to observe individual peaks from the free excitons. Therefore, to understand more about the properties of defect related and excitonic emissions of the nanowires/nanorods, low temperature photoluminescence measurements are essential. At low temperature, there will be better resolution of these multiple peaks as the thermal broadening effect and electron/exciton-phonon interactions will be strongly reduced. The

thermal ionization effect on the defects will also be reduced and hence the defect properties will be easily identified. Furthermore, by analysing the results of the room temperature and low temperature (12 K) excitation and emission spectra of the nanowires, together with the growing conditions, it will be relatively straightforward to suggest and specify possible candidates for defect related emissions of the nanowires/nanorods. Section 4.2.3.2 deals with the low temperature excitation and emission properties of the nanowires.

Qualitative information about the effect of the parameters such as substrate temperature and O_2 flow rate on the emission spectra of the nanowires/nanorods can be inferred from the comparison of their emission spectra. The nanowires and nanorods on Si substrates had different substrate temperature and flow rate of O_2 during the growth. As it is mentioned previously, the GL and UV bands of the nanowires/nanorods do not show any measurable change in peak position for the entire excitation wavelengths used. However, the intensity of these bands is higher for the nanowires grown with relatively higher flow rate of O_2 as shown in Fig. 4-14. One reason for the variation in intensity can be attributed to the relative amount of O_2 because O_2 excess or deficit affects the quality of the samples and hence the resulting emission spectra. In the XRD spectra, it has been also shown that the intensity of the diffraction peaks from the nanowires was smaller and the 2θ values of these peaks showed larger deviation than that of the nanorods grown with lower O_2 flow rate, suggesting that more O_2 related defects were likely formed in the nanowires. The other reason may be due to the differences in surface morphology which influences the emission spectra of the nanowires and nanorods. From the SEM images, the nanowires and nanorods have different morphologies and this can be also resulted from the amount of O_2. For example, in the works of C. Wang et al. [62] it has been demonstrated that ZnO thin films grown under different amount of O_2 had different surface structure and roughness which significantly changed the emission spectra of the films. Moreover, the GL band is centered at ~2.45 eV for both the nanowires and nanorods, indicating that a common type of defect is likely responsible for the origin of the GL from the as-grown nanowires and nanorods. Hence, the only difference in the emission intensity of the nanowires and nanorods might result from the relative variation in the concentration of the same defect they contain. In this case, O_2 may play the role for the variation of the defect concentration. For instance, X. M. Teng et al. [58] have investigated the effect of oxygen partial pressure,

P_{O2}, on the emission spectra of as-grown ZnO thin films on Si substrate. In the result they found that the emission intensity increases with increasing the P_{O2} and reaches a maximum at an optimal value of P_{O2} and then decreases again with almost the same peak position. This finding is in agreement with the observed intensity differences between the emission spectra of the nanowires and nanorods. The nanowires which were grown with relatively higher O_2 flow rate have showed relatively higher intensity for the entire excitation wavelengths used. Furthermore, the nanorods and nanowires were grown at different substrate temperatures, Substrate-I and Substrate-II, respectively. This has also a prominent effect on the emission spectra as it influences the morphology and structure of the as-grown nanostructures. The above results reveal that the emission intensity of the as-grown nanowires and nanorods can be influenced by the synthesis parameters such as flow rate of gases and substrate temperature. However, it should be noted that intensity also depends on other factors like absorption cross-section of the samples [60] and hence quantitative measurements such as emission quantum yield have to be employed in order to support the interpretation on the observed intensity differences between the emission spectra of nanowires and nanorods.

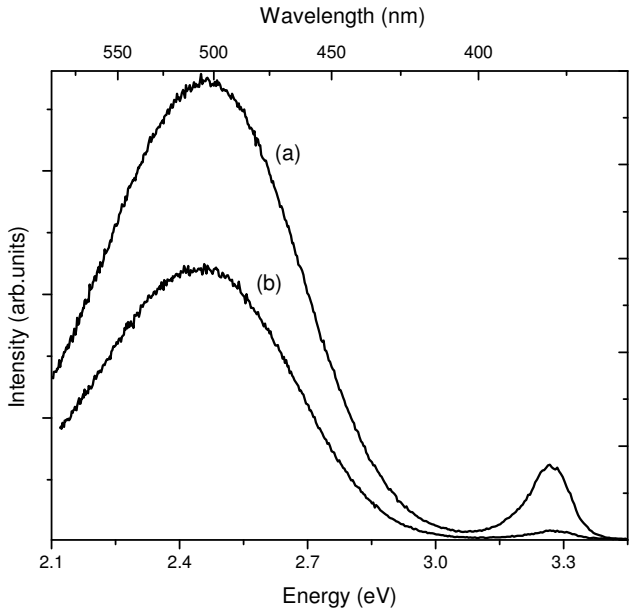

Fig. 4-14. Room temperature emission spectra of the (a) nanowires and (b) nanorods on Si substrate, excited at 312 nm (3.94 eV).

4.2.3.2. Photoluminescence Spectra of Nanowires at Low Temperature (12 K)

The low temperature (12 K) excitation spectra of the nanowires on Si substrate have been measured by monitoring the emission at different wavelengths. The excitation spectra shown in Fig. 4-15 have very different features from the corresponding spectra measured at room temperature (Fig. 4-11b). At 12 K several transition (absorption) lines that were quenched at room temperature can be seen in the excitation spectra. Each excitation spectrum consists of a series of peaks which correspond to the energy greater than the band gap energy of ZnO. This implies that all the possible transitions such as the exciton, bound exciton, DAP and defect related transitions can participate and thus the observed peaks in the excitation spectra are attributed to these transitions. In addition, the excitation bands at the monitored emission wavelengths (366 and 374 nm) in the UV spectral region are more dominant over the excitation bands monitored in the visible region (420 and 500 nm). Therefore, unlike the room temperature UV bands which were relatively weak, it can be expected that the UV bands at 12 K will be the predominant bands in the corresponding emission spectra of the nanowires.

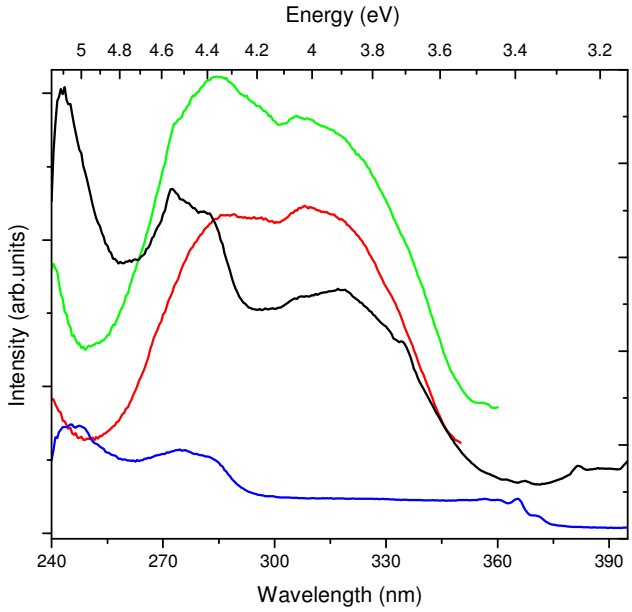

Fig. 4-15. Low temperature (12 K) excitation spectra of the nanowires on Si substrate, the emission wavelengths being monitored at 366 nm (red color), 374 nm (green color), 420 nm (black color) and 500 nm (blue color).

Having the information from the excitation spectra of Fig. 4-15, the sample was then excited at various excitation wavelengths (photon energies) corresponding to the excitation maxima of the spectra. Several fine structures that correspond to the peaks in the excitation spectra can be seen in most of the emission spectra as seen in Fig. 4-16. Due to the effect of low temperature, the emission spectra here show very different features compared to the corresponding room temperature emission spectra in Fig. 4-12b. For instance, two new bands peaking at about 2.90 and 3.06 eV can be seen for excitation wavelengths 240 nm (5.17 eV) and 365 nm (3.40 eV), respectively, (Fig. 4-16). For the purpose of easy comparison on all emission features, the emission spectra have been scaled to the same peak height as in Fig. 4-16.

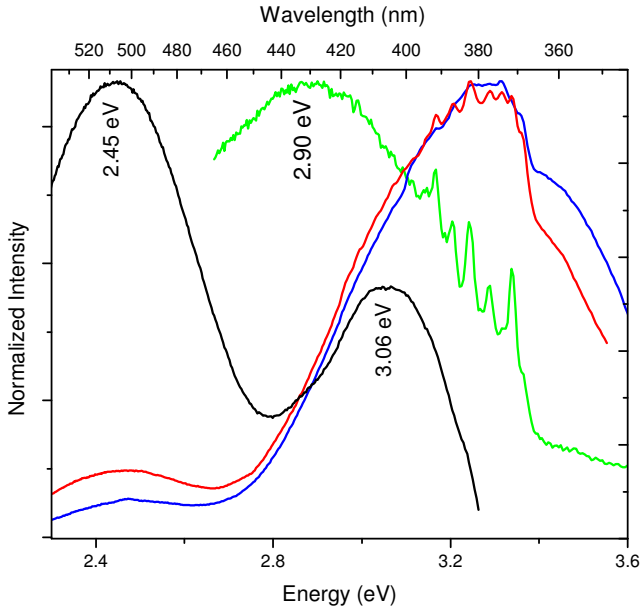

Fig. 4-16. Low temperature (12 K) emission spectra of the nanowires on Si substrate, excited at different wavelengths: 240 nm (green color), 305 nm (blue color), 334 nm (red color), 365 nm (black color).

From Fig. 4-16 we can observe common features as well as differences among the structures in the emission spectra obtained by different excitation wavelengths (excitation energies). For the UV bands, most of the emission spectra contain a series of well resolved fine emission peaks and the positions of such peaks do not change as the excitation wavelength (energy) changes (Fig. 4-16). However, the number of peaks in each spectrum and their intensity varies nonlinearly as the excitation wavelength varies. For excitation

wavelengths (energies) 240 and 334 nm (5.16 and 3.71 eV), seven peaks positioned at ~3.1673, 3.2041, 3.2418, 3.2891, 3.3155, 3.3378, and 3.3604 eV can be clearly observed. The seven peaks can be also seen for excitation wavelengths (energies) 305 nm (4.06 eV) and 316 nm (3.92 eV) but in this case it is difficult to identify easily some of the peaks as their bands get broadened and merged together. Particularly, at excitation wavelength of 284 nm (4.37 eV), only the three peaks centered at ~3.2418, 3.3155 and 3.3604 eV were observed (not shown in the figures). The assignment of these peaks will be discussed later in this section. Fig. 4-17 shows the characteristics of the emission peaks for excitation wavelengths (energies) 316 nm (3.92 eV) and 334 nm (3.71 eV).

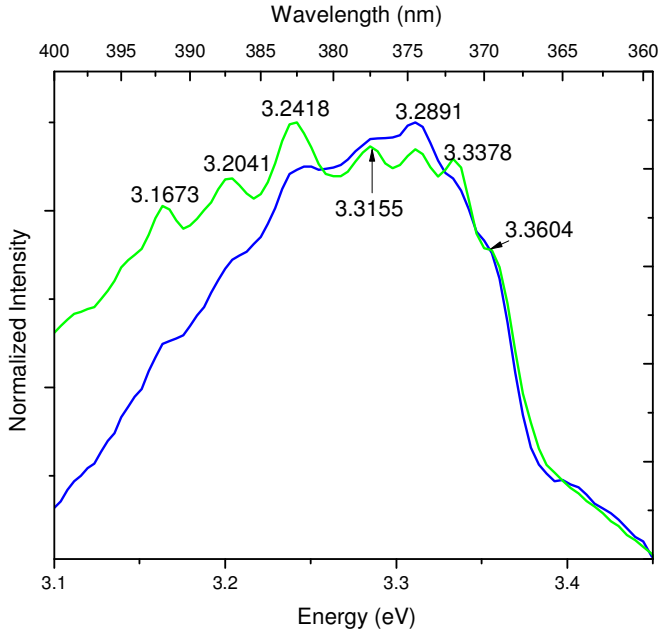

Fig. 4-17. Emission spectra of nanowires on Si substrate at 12 K, excited at 316 nm (blue color) and 334 nm (green color).

Unlike the room temperature, the UV band at 12 K extends in a very broad range of energies for all excitation wavelengths used and its relative intensity is higher. For instance, for the excitation wavelength 334 nm (3.71 eV) the fwhm of the UV band at 12 K is ~575 meV which is about 5 times greater than its corresponding fwhm (110 meV) at room temperature. Fig. 4-18 represents the normalized room temperature and 12 K emission spectra of the nanowires on Si substrate, at excitation wavelength 334 nm (3.71 eV).

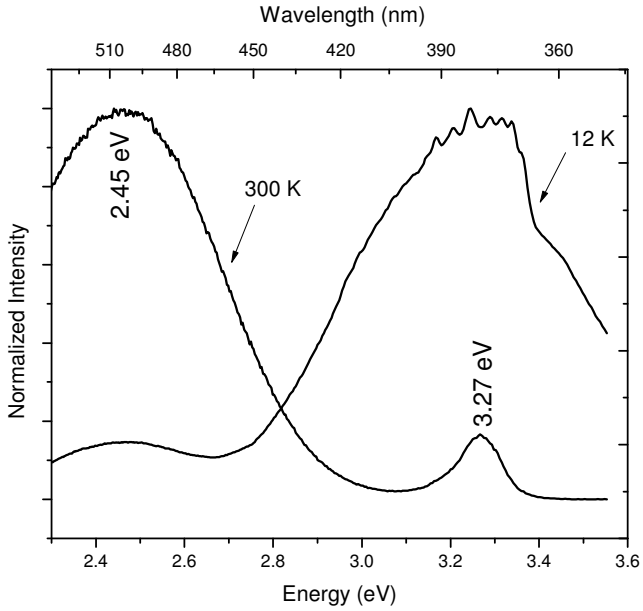

Fig. 4-18. Room temperature and low temperature emission spectra of the nanowires on Si substrate, excited at 334 nm (3.71 eV).

Referring to Table-1 and the discussions in section 2.3, the observed peaks in Fig. 4-17 do not correspond to the free exciton transition lines in ZnO. Here, the broadness of the UV band without clear observation of any free exciton transition line can be resulted from the existence of various defects in the band gap, with high level of concentration. As it has been mentioned in section 2.3, if the sample consists of several defects, the excitons will no longer remain free but they are bounded by the defects and hence observation of peaks from free exciton transitions will be improbable. Instead, bound exciton (BX), DAP and their phonon replica transitions will be the predominant bands covering wide range of energies depending on the type and density of defects available. This is because of the fact that at low temperatures excitons are highly localized by the defects (impurities) as it has been confirmed experimentally via temperature dependent emission spectra of ZnO nanowires [30,40], nanorods [38,33], films [21,25] and bulks [27,36,39]. In the reported literatures, it has been observed that the intensity of bound exciton and DAP emissions decreases with an increase in the temperature and finally quenches above a certain temperature value, confirming that bound excitons and impurities are thermally ionized at high temperatures. As it can be seen in Fig. 4-16, the appearance of the new bands positioned at ~2.90 and 3.06 eV might be consequences of such effects and thus the bands can be attributed to the defect related transitions which were quenched at room temperature

due to the ionization of the defects. Hence at low temperature, the localization of free excitons is expected in a sample where various defects with high level of concentration exist and the emission will be dominated by the bound excitons as well as the DAP and their phonon assisted transitions, in broad energy ranges. In this case, it will be difficult to observe sharp and narrow lines of free excitons; even if there is a transition of them the peak will be very weak and unresolved. Such observation have been also reported in typical ZnO films or bulk crystals in which the free exciton band is not clearly observed at low temperatures due to the localization of excitons by impurities, especially donors, ref(14) in [41]. A. Mohanta et al. [30] also reported temperature dependent emission profile measured in the $\mathbf{E}\perp\mathbf{c}$ polarization geometry of ZnO nanowires grown by thermal evaporation. In this study the dominant peak (3.354 eV) in the broad UV band at 6 K was assigned to the bound exciton (BX) transition which disappeared above the temperature of 150 K. Though some peaks are not clearly seen, for example the A free exciton ($FX_A^{n=1} = 3.375\,eV$), the Gaussian fitting indicated that the broad band in the UV spectral region contains seven peaks (Fig. 2-3). On the other hand, for relatively high quality samples well resolved free exciton lines, their excited states, phonon replicas and bound exciton transitions can be clearly observed within narrow ranges of energies in the low temperature emission spectra of ZnO samples. For instance, Teke et al. [27] have reported the emission spectra measured in the $\mathbf{E}\perp\mathbf{c}$ polarization geometry at 10 K of a high quality ZnO crystal samples and classified the spectrum as free exciton (3.374-3.480 eV), bound exciton (3.348-3.374 eV), two-electron-satellite (3.32-3.34 eV) and DAP and LO phonon replica (2.95-3.32 eV) regions. Moreover, each region consists of several number of clearly observable emission lines. As such, several neutral bound exciton emission lines (acceptor and donor bound excitons of A and B excitons) have been observed in the bound exciton region where the dominant peak (3.3605 eV) of the whole emission spectrum is found (Fig. 2-6).

Based on previously reported literatures, the observed peaks in the emission spectra of Fig. 4-17 could be assigned to the most likely transition lines. The peak at ~3.3604 eV is commonly referred to the bound exciton (BX) transition line by many authors [20,21,27,38,40,41]. Teke et al. [27] had assigned it specifically to the A exciton bound to a neutral donor in the second excited state ($D^o_2\ X_A$). While the peak at ~3.3378 eV in the

region of two-electron-satellite (TES) transition lines might be attributed to TES transitions of the bound exciton (BX) or possibly excitons bound to structural defects [21,33]. However, the donor binding energy, E_D, ~30.1 meV calculated from the energy separation between the BX and TES lines shows large deviation from the corresponding value ~53 meV reported in [20,27]. Hence the line at ~3.3378 eV could not be related to TES rather it might be due to defects. At low temperature the LO phonon replica transition lines of ZnO occur within a separation of 71-73 meV [21]. Hence based on such energy separation, the emission line at ~3.2891 eV located 71.5 meV away from the BX line can be assigned to the first LO phonon replica of the bound exciton, BX-1LO. This is also in good agreement with the assignment given by Teke et al. [27]. Another peak at ~3.3155 eV can be ascribed to the donor acceptor pair (DAP) emissions [40]. Detail study of low temperature emission spectra of high quality ZnO nanorods on sapphire substrates can be found in [33]. In this study, the same peak at 3.3155 eV has been observed (Fig.2-5) and it is assigned to a DAP transition line. Again if the energy separation between the peaks is considered, ~74 meV, the emission lines at ~3.2418 eV and 3.1673 eV can be related to the first and second order phonon replicas of the DAP transitions, DAP-1LO and DAP-2LO, respectively. The assignments of these peaks are consistent with those reported in [40,33]. Finally, the peak at ~3.2041 eV and other peaks which are found in the DAP and LO phonon replica regions could be attributed to the DAP, defect or defect complex emissions. However, the chemical origin of the donor and acceptor atoms (impurities) associated with the DAP and BX transitions are still unclear [20,21,32] though DAP, bound exaction and defect emissions of ZnO are reported by many research groups. Furthermore, the information obtained from the emission spectra here might not be enough to assign the peaks because the sample seems to have several defects. In this case additional information about the behaviour and origin of the peaks is required so that the assignment of peaks will be more accurate. For instance, Electron Paramagnetic Resonance (EPR), Hall-effect measurements, Secondary Ion Mass Spectrometry (SIMS), and even varieties of emission techniques such as time resolved and temperature dependent emission spectra are very helpful in identifying the chemical nature of the defects involved and the recombination mechanisms behind each transition.

Another feature of the emission spectra at 12 K is the property of the GL band. Contrary to the room temperature emission spectra in which the GL band was the dominant peak, almost for all excitation wavelengths, here the GL band is highly suppressed by that of the UV band as it is shown in Fig. 4-16. However, the relative intensity of the GL at 12 K is still higher than that of its intensity at room temperature but no significant change in peak position (~2.45 eV) is observed. The emission spectra of the GL bands at room temperature and 12 K for an excitation wavelength of 365 nm (3.40 eV) are presented in Fig. 4-19. In the figure it can be seen that both the 12 K and room temperature GL bands display Gaussian features with fwhm about 466 and 524 meV, respectively. Here, the manifestation of a relatively narrow fwhm with higher relative intensity can be the result of the lower temperature effects in which phonon interactions and probabilities of carriers to recombine nonradiatively are expected to be reduced. Furthermore, the appearance of another Gaussian characteristic band peaking at ~3.06 eV indicates that the defects responsible for this band were ionized or quenched at room temperature.

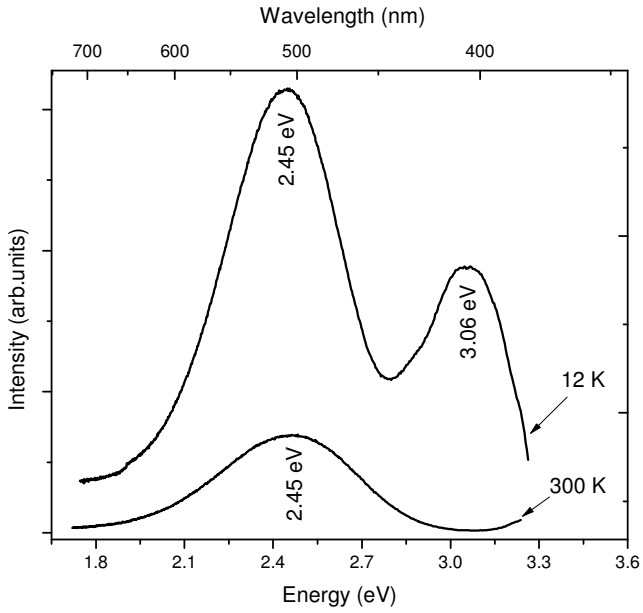

Fig. 4-19. Room temperature and low temperature emission spectra of the nanowires on Si substrate, excited at 365 nm (3.40 eV).

Though the assignment of defect emissions in ZnO to specific defects is often controversial, from the results of room temperature and 12 K emission spectra it can be suggested that the GL band likely originates from a single type of defect related emission. The Gaussian

nature of the band will make a DAP transition to be a possible candidate for the emissions of GL because the DAP transition is commonly characterised by a nearly Gaussian broad band which shows a small decrease in the fwhm, and a moderate increase in the intensity with the decrease of temperature, ref(56) in [38]. The other most widely proposed hypothesis for the origin of GL is the recombination of photoexcited hole and an electron at a single ionized oxygen vacancy [26,35,40]. On the other hand, after detail analysis of the photoluminescence properties of ZnO nanostructures, B. Aleksandra et al. [65] have concluded that the origin of the green luminescence is most likely from multiple defects and/or defect complexes rather than a single ionized oxygen vacancy. They have also investigated that the green luminescent intensity was significantly reduced when the as-grown nanostructures were coated, showing that the major part of the green emission originates from surface defects. In a similar work, D. Li et al. [63] have found that the green emission of ZnO nanostructures fabricated by thermal evaporation method was significantly suppressed after coating the samples with a surfactant. In general, the exact chemical nature of the defects responsible to the luminescent features is still a debate [20,32]. The identification will be relatively unambiguous in conditions where different characterisation techniques are employed for the same sample grown in well controlled conditions. In this work, to propose the possible candidates for the defect related emissions first we have to examine the growth parameters and then correlate them with results of the characterisations. Accordingly, due to the variation of different parameters such as temperature, flow rate of gases and synthesis time during the growth of the nanowires, the concentrations of oxygen vacancies, interstitials and antisites as well as that of Zn may vary leading to the nonstoichiometry of ZnO. This can be interpreted as follow: during the synthesis time the nucleation and growth of the nanowires were going under high flow of oxygen at a constant rate. In addition, oxygen was flowing with this constant rate while the furnace was cooling down to room temperature. During the cooling process the amount of Zn vapor obviously decreases as the temperature of the source is decreasing (see Fig. 3-3 for the relation). These situations imply that the nanowires were more likely exposed to excess oxygen during the entire nucleation and growth processes. Under O_2 rich ambient the formation energy of Zn vacancies (V_{Zn}), oxygen interstitials (O_i) and oxygen antisites (O_{Zn}) are lower than that of oxygen vacancies (V_O), Zn antisites (Zn_O) or Zn interstitials (Zn_i) [8,26]. Hence, the most likely defects that could be formed in the nanowires will be

V_{Zn}, O_{Zn}, O_i and their complexes. However, the XRD spectra show the presence of Zn impurity which is most probably resulted from the sprinkled Zn particles or (though less probably) from unreacted Zn vapor, suggesting that the nanowires have some Zn_i in spite of the fact that the formation energy of Zn_i under excess oxygen is unlikely [8,26]. Therefore, based on these analyses, previously reported literatures and the theoretically calculated defect energy levels in ZnO, the most likely candidates for the emissions at ~3.06, 2.90 and 2.45 eV are V_{Zn}, Zn_i, and O_{Zn}, respectively, Fig. 2-7. An alternative candidate for the emission of GL at ~2.45 eV might also be surface defects, as it has been observed that surface coating of the as-grown samples changes the properties of the GL [63,65].

Chapter 5:

5.1. Conclusions and Future Perspectives

ZnO is a direct and wide band gap (3.37 eV) semiconductor with large exciton binding energy (60 meV) at room temperature. It has received an increasing attention due to its potential applications in the future nano-electronic and optoelectronic devices as well as piezoelectric, biosensor and spintronic devices. The wide applications of ZnO could be practically achieved by following appropriate synthesis routes and studying the optical, electrical, thermal and mechanical properties of the resulting nanostructures. Accordingly, in this work, ZnO nanowires/nanorods have been grown on Al_2O_3 and Si substrates by thermal evaporation at atmospheric pressure without using any catalyst or additive. The synthesis route is simple and environmentally friendly. Metallic Zn powder was heated at a temperature above its melting point. The vapor was then transported by the help of the temperature gradient and nitrogen gas to the substrates placed down in the lower temperature regions. As oxygen was also flowing in the tube, it would react with the vapor and ZnO nanostructures grew on the substrates. The morphology, crystal structure and optical features of the as-grown nanowires/nanorods were characterised by SEM, XRD, and photoluminescence spectroscopy, respectively.

The SEM images reveal that the morphologies of the nanowires/nanorods were highly influenced by the growth conditions such as temperature, flow rate of gases, and substrate. Temperature and gas flow rates were the major determining factor for the growth and morphologies of nanowires/nanorods. Both of them influence the supersaturation level of the vapor on the source and substrates. If the source temperature is high then much vapor will be produced. However, the amount of vapor reaching the substrates depends mainly on the flow rate of the carrier gas. The higher the flow rate, the longer does the vapor would be transported before it gets deposited on the substrates. Hence, with high flow rate of carrier gas the optimal growth of nanowires/nanorods were found at a relatively far distance from the source material. It is also important to determine the critical flow rate of oxygen for optimal growth of nanowires/nanorods. For high flow rate of oxygen the Zn vapor immediately reacts with oxygen and eventually forms ZnO layer on the surface of

the source. Consequently, further evaporation of Zn from the source will be impeded and growth of the nanowires/nanorods terminates. The growth of the seeds on the substrates is affected by the grains, cracks, and steps of the substrates as well as the sprinkled particles. On the other hand, the nanowires/nanorods were seen to grow from the surfaces of the seeds. Therefore, the growth of the nanowires/nanorods was indirectly influenced by the substrate surface. Substrate temperature was the other factor which has played a prominent role on the morphology of the nanowires/nanorods.

Results of the X-ray diffraction indicate that the as-grown nanowires/nanorods have a wurtzite structure of bulk ZnO. However, impurities of Zn which might be resulted from the unreacted Zn vapor or sprinkled Zn powder have been observed on nanowires and nanorods grown on Si substrates. It has been also observed that the relative intensity and position of the diffraction peaks have slight differences among the nanowires/nanorods, indicating that the growth parameters have effects on the crystal quality of the resulting structures.

The fact that there was no metal catalyst used in the synthesis combined with the SEM and XRD results leads to a conclusion that the most likely growth mechanism of the nanowires/nanorods is VS mechanism. As seen in the SEM images the nanowires/nanorods extend outward from the surfaces of the seeds and are randomly oriented, showing the behaviour of VS growth mechanism. Furthermore, no diffraction peaks of other metal impurities were seen in the XRD spectra of the samples.

The room temperature excitation and emission spectra have been investigated to understand the optical qualities and properties of the as-grown nanowires and nanorods. Additional information about the optical properties has been obtained from the low temperature (12 K) excitation and emission spectra of the nanowires grown on Si substrate.

At room temperature, the emission spectra of the nanowires/nanorods showed characteristics of two well structured bands, the green luminescence (GL) and UV bands. The GL is attributed to the defects while the UV band is due to phonon assisted excitonic emissions. In all cases, the GL band is the dominant peak over the entire emission spectra

indicating that the nanowires/nanorods have considerable defects. Defects are formed during the growth of the nanowires/nanorods due to the effects of several parameters such as temperature and gas flow rates.

The low temperature (12 K) excitation and emission spectra of the nanowires on Si substrate have very different features compared to the corresponding spectra at room temperature. The excitation spectra consist of several peaks corresponding to the various defect energy levels in the band gap and bound exciton transition lines (absorptions). The corresponding emission spectra confirm the presence of impurities (defects) in the nanowires. No clear observation of the free exciton transition lines could be detected. Instead, the entire emission spectrum is dominated by a broad UV band containing several fine structure transition lines which are attributed to the bound exciton, DAP, LO phonon replicas, defects and defect complexes. Further more, the GL band is highly suppressed by the UV band but its peak position remains nearly unchanged. In addition to the GL band, two Gaussian characteristic bands peaking at ~2.90 and 3.06 eV appeared for excitation wavelengths 240 and 365 nm, respectively. Based on the theoretically calculated defect energy levels in ZnO and the growth conditions, we conclude that the emission peaks at ~ 2.90 and 3.06 eV are due to transitions from Zn interstitials (Zn_i) to valance band and from conduction band to Zn vacancy (V_{Zn}), respectively. The GL at ~2.45 eV can be related either to oxygen antisite (O_{Zn}) or to surface defects.

Finally, the SEM images, XRD data and photoluminescence features coupled with comparison of the results with related literatures lead to the conclusion that the nanowires are highly subjected to several defects and their complexes, with high level of concentration. However, the exact chemical nature of the defects responsible for the luminescent features has not been resolved yet. The identification of the luminescent centers will be unambiguous in conditions where various characterisation techniques are employed, together with controlled growth of the samples and it would be a subject of further investigation.

- Further work on the identification of the specific defects is indispensable for the application of ZnO nanostructures to the desired device. If the exact sources of defect emissions are identified it will be possible to create or avoid defects intentionally during the growth or after growth so that the luminescent properties of the defects can be tuned depending on the needs. For instance, to fabricate optoelectronic devices working in the visible spectral region an intentional creation of the desired defect will be a must. On the other hand, all unintentionally created defects must be eliminated if the nanostructures are to be used in semiconductor lasers and UV-emitting devices. In general, for complete identification of the defects a comprehensive study is essential so that the wide applications of ZnO can be achieved.

- In the semiconductor industry it is well know that Si is the most widely used semiconductor material. Therefore, the fabrication of ZnO nanowires/nanorods on Si substrates and full understanding of their electrical, optical, thermal and mechanical properties will provide a possibility of integrating these nanostructures with Si based nanoscale devices, which will make great contributions towards device miniaturization of integrated circuits.

References

[1] Mark A. Reed, Quantum dots, *Scientific American*, 268, 118-123, 1993.

[2] Z. R. Dai, Z. W. Pan, and Z. L. Wang, Novel Nanostructurs of Functional Oxides Synthesized by Thermal Evaporation, *Advanced Functional Materials*, 13, 9-23, 2003.

[3] Y. Zhang, N. Wang, S. Gao, R. He, S. Miao, J. Liu, J. Zhu and X. Zhang, A Simple Method to Synthesize Nanowires, *Chemistry of Materials*, 14, 3564-3568, 2002.

[4] P. Yang, H. Yan, S. Mao, R. Russo, J. Johnson, R. Saykally, N. Morris, J. Pham, R. He and H. -J. Choi, Controlled Growth of ZnO Nanowires and Their Optical Properties, *Advanced Functional Materials*, 12, 323-330, 2002.

[5] Z. L. Wang, ZnO Nanostructures: Growth, Properties and Applications, *Journal of Physics: Condensed Matter,* 16, R829-R858, 2004.

[6] Zhong Lin Wang, Nanostructures of ZnO, *Materials Today*, 7, 26-33, 2004.

[7] Pu Xian Gao and Zhong L. Wang, Nanoarchitectures of semiconducting and piezoelectric ZnO, *Journal of Applied Physics*, 97, 044304 (7), 2005.

[8] S. M. Lukas and M. D. Judith L., ZnO - nanostructures, defects, and devices, *Materials Today*, 10, 40-48, 2007.

[9] P. X. Gao and Z. L. Wang, Nanoarchtecture of Semiconducting and Piezoelectric ZnO, *Journal of Applied Physics*, 97, 044304 (7), 2005.

[10] X. Yang and Z. L. Wang, Spontaneous Polarization-induced Nanohelexes, Nanosprings, and Nanorings of Piezoelectric Nanobelts, *Nano Letters*, 3, 1625-1631, 2003.

[11] Z. Fan and J. G. Lu, ZnO Nanostructures: Synthesis and Properties, *nami.usc.edu/file.php/1/publications/29.pdf,* retrieved on 20 Nov. 2008.

[12] W. II Park, J. S. Kim, G. C. Yi, M. H. Bae and H. J. Lee, Fabrication and electrical characteristics of high-performance ZnO nanorod field-effect transistors, *Applied Physics Letters*, 85, 5052 (3), 2004.

[13] R. Yakimova, Developments in the growth of wide band gap semiconductors, *Physica Scripta*, T126, 121–126, 2006.

[14] Z. Fan and J. G. Lu, Nanostructured ZnO: Building Blocks for Nanoscale Devices, *International Journal of High Speed Electronics and Systems,* 16, 883-896, 2006.

[15] P. C. Chang, Z. Fan, D. Wang, W. Y. Tseng, W. A. Chiou, J. Hong and J. G. Lu, ZnO Nanowires Synthesised by Vapor Trapping CVD Method, *Chemistry of Materials,* 16, 5133-5137, 2004.

[16] Y. Q. Chang, D. B. Wang, X. H. Luo, X. Y. Xu, X. H. Chen, L. Li, C. P. Chen, R. M. Wang, J. Xu, D. P. Yu, Synthesis, Optical, and Magnetic Properties of Diluted Magnetic Semiconductor $Zn_{1-x}Mn_xO$ Nanowires via Vapor Phase Growth*, Applied Physics Letters*, 83, 4020-4023, 2003.

[17] Simon L. Altmann*, Band Structure of Solids: An Introduction from the Point of View of Symmetry*, Oxford University Press Inc., New York, 1995.

[18] http://en.wikipedia.org/wiki/Wurtzite, retrieved on 20 Feb. 2009.

[19] D. C. Reynolds, D. C. Look, B. Jogai, C. W. Litton, G. Cantwell, W. C. Harsch,Valence-band ordering in ZnO, *Physical Review B,* 60, 1240-1244, 1999.

[20] B. K. Meyer, H. Alves, D. M. Hofmann, W. Kriegseis, D. Forster, F. Bertram, J. Christen, A. Hoffmann, M. Strassbburg, M. Dworzak, U. Haboeck, and A. V. Rodina, Bound exciton and donor–acceptor pair recombinations in ZnO, *Physica Status Solidi. B. Basic Research,* 241, 231-260, 2004.

[21] Ü. Özgür, Ya. I. Alivov, C. Liu, A. Teke, M. A. Reshchikov, S. Doğan, V. Avrutin, S. -J. Cho, and H. Morkoç, A comprehensive review of ZnO materials and devices, *Journal of Applied Physics,* 98, 041301 (103), 2005.

[22] D. C. Reynolds, C. W. Litton, T. C. Collins, J. E. Hoelscher, and J. Nause, Observation of donor-acceptor pair spectra in the photoluminescence of H- and Zn-implanted ZnO single crystals, *Applied Physics Letters*, 88, 141919 (3), 2006.

[23] C. Klingshirn, ZnO: From basics towards applications, *Physica Status Solidi. B. Basic Research*, 244, 3027-3073, 2007.

[24] W. R. Lambrecht, A. V. Rodina, S. Limpijumnong, B. Segall, B. K. Meyer, Valence-band ordering and magneto-optic exciton fine structure in ZnO, *Physical Review B*, 65, 075207 (12), 2002.

[25] S. Adachi, Polarization and wave-vector-dependent measurements by four-wave mixing in ZnO: valence-band ordering and biexcitons, *Journal of Luminescence*, 112, 34-39, 2005.

[26] A. Janotti and C. G. Van de Walle, Native point defects in ZnO, *Physical Review,* 76, 165202 (22), 2007.

[27] A. Teke, Ü. Özgür, S. Dogan, X. Gu, H. Morkoç, B. Nemeth, J. Nause, and H. O. Everitt, Excitonic fine structure and recombination dynamics in single-crystalline ZnO, *Physical Review B* , 70, 195207 (10), 2004.

[28] Mark Fox, *Optical Properties of Solids*, Oxford University Press, 2001.

[29] J. I. Pankove, *Optical Processes in Semiconductors*, Dover Publications, Inc., N.Y., 1971.

[30] A. Mohanta and R. K. Thareja, Photoluminescence study of ZnO nanowires grown by thermal evaporation on pulsed laser deposited ZnO buffer layer, *Journal of Applied Physics*, 104, 044906 (6), 2008.

[31] Y. P. Varshni, Temperature dependence of the energy gap in semiconductors, *Physica,* 34, 149-154, 1967.

[32] J. Liu, S. Lee, Y. H Ahn, J. Y Park and K. Ha Koh, Tailoring the visible photoluminescence of mass-produced ZnO nanowires, *Journal of Physics D: Applied Physics*, 42, 095401 (6), 2009.

[33] B. P. Zhang, N. T. Binh, Y. Segawa, K. Wakatsuki, and N. Usami, Optical properties of ZnO rods formed by metalorganic chemical vapor deposition, *Applied Physics Letters*, 83, 1635-1637, 2003.

[34] B. Lin, Z. Fu, and Y. Jia, Green luminescent center in undoped ZnO films deposited on silicon substrates, *Applied Physics Letters*, 79, 943-945, 2001.

[35] L. Yang, J. Yang, D. Wang, Y. Zhang, Y. Wang, H. Liu, H. Fa, and J. Lang, Photoluminescence and Raman analysis of ZnO nanowires deposited on Si(100) via vapor–liquid–solid process, *Physica E*, 40, 920–923, 2008

[36] H. Zhong, X. Chen, L. Z. Sun, W. Lu, Q. X. Zhao, and M. Willander, A novel photoluminescence transition influenced by O implantation in ZnO bulk, *Chemical Physics Letters*, 421, 309-311, 2006.

[37] H. C. Hsu, and W. F. Hsieh, Excitonic polaron and phonon assisted photoluminescence of ZnO nanowires, *Solid State Communications*, 131, 371-375, 2004.

[38] A. B. Djuriˇsi´, Y. H Leung, K. H Tam, Y. F Hsu, L. Ding, W. K Ge, Y. C Zhong, K. S Wong, W. K Chan, H. L Tam, K. W Cheah, W. M Kwok, and D. L Phillips, Defect emissions in ZnO nanostructures, *Nanotechnology*, 18, 095702 (8), 2007.

[39] L. Wang and N. C. Giles, Temperature dependence of the free-exciton transition energy in ZnO by photoluminescence excitation spectroscopy, *Journal of Applied Physics*, 94, 973-978, 2003.

[40] Z. M. Liao, H. Z. Zhang, Y. B Zhou, J. Xu, J. M. Zhang, and D. P. Yu, Surface effects on photoluminescence of single ZnO nanowires, *Physics Letters A*, 372, 4505-4509, 2008.

[41] S. W. Kim, Shizuo Fujita, and Shigeo Fujita, ZnO nanowires with High Aspect ratios grown by metalorganic chemical vapor deposition using gold nanoparticles, *Applied Physics letters*, 86, 153119 (3), 2005.

[42] Y. C. Kong, D. P. Yu, B. Zhang, W. Fang, and S. Q. Feng, Ultraviolet-emitting ZnO Nanowires Synthesized by a Physical Vapor Deposition Approach, *Applied Physics letters*, 78, 407-409, 2001.

[43] T. Y. Kim, S. H. Lee, K. S. Nahm, J. Y. Kim, H. W. Shim, E. K. Suh, and *S.* H. Lee, Catalytic Growth and Characterisation of ZnO Nano-needles, *Nanotechnology*, 2, 823-827, 2003.

[44] J. Y. Kim, H. W. Shim, E. K. Suh, T. Y. Kim, S. H. Lee, Y. H. Mo and K. S. Nahm, Catalytic Growth and Optical Characterisation of ZnO Nanowire on Silicon and Sapphire, *Journal of the Korean Physical Society*, 44, 137-139, 2004.

[45] L. Vayssieres, Growth of Arrayed Nanorods and Nanowires of ZnO from aqueous Solution, *Advanced Materials*, 15, 464-466, 2003.

[46] S. Bu, C. Cui, Q. Wang, and L. Bai, Growth of ZnO Nanowires in Aqueous Solution by a Dissolution-Growth Mechanism, *Journal of Nanomaterials*, 2008, 1-5, 2008.

[47] A. M. Morales and C. M. Lieber, A Laser Ablation Method for the Synthesis of Crystalline Semiconductor Nanowires, *Science,* 279, 208-211, 1998.

[48] D. R. Gaskell, *Introducition to Metallurgical Thermodynamics*, 2nd Ed, Hemisphere Publishing, Washington, DC, 1986.

[49] Y. Xia, P. Yang, Y. Sun, Y. Wu, B. Mayers, B. Gates, Y. Yin, F. Kim, and H. Yan, One-Dimensional Nanostructures: Synthesise, Characterisation, and Applications, *Advanced Materials*, 15, 353-389, 2003.

[50] X. Zhang, L. Wang and G. Zhou, Synthesise of Well-Aligned ZnO Nanowires without Catalysts, *Reviews of Advanced Materials Science (RAMS)*, 10, 69-72, 2005.

[51] R. S Wagner and W. C Ellis, Vapor-Liquid-Solid Mechanism of Single Crystal Growth, *Applied Physics Letters*, 4, 89-90, 1964.

[52] C. Y. Lee, T.Y. Tseng, S.Y. Li and P. Lin, Growth of ZnO Nanowires on Silicon (100), *Tamkang Journal of Science and Engineering*, 6, 127-132, 2003.

[53] Shulin JI and Changhui YE, Synthesis, Growth Mechanism, and Applications of ZnO Nanomaterials, *Journal of Materials Science and Technology,* 24, 457-472, 2008.

[54] G. Shen, Y. Bando, B. Liu, D. Golberg, and C. J Lee**,** Characterisation and Field-Emission Properties of Vertically Aligned ZnO Nanonails and Nanopencils Fabricated by a Modified Thermal-Evaporation Process, *Advanced Functional Materials,* 16, 410-416, 2006.

[55] A. Umar, Y. H. Im, and Y. B. Hahn, Evolution of ZnO Nanostructures on Silicon Substrate by Vapor–Solid Mechanism: Structural and Optical Properties, *Journal of Electronic Materials*, 35, 758-765, 2006.

[56] Mónica Morales Masís, *Fabrication and Study of ZnO Micro- and Nanostructures,* A thesis submitted in partial fulfilment of the requirements for the degree of Master of Science, Wright State University, Dayton-Ohio, 2007.

[57] G. Cao, *Nanostructures & Nanomaterials; synthesis, properties & application*, Imperial College press, London, 2004.

[58] X. M. Teng, H. T. Fan, S. S. Pan, C. Ye and G. H. Li, Photoluminescence of ZnO thin films on Si substrate with and without ITO buffer layer, *Journal of Physics D: Applied Physics*, 39, 471-476, 2006.

[59] L. Xu, L. Shi, and X. Li, Effect of TiO_2 buffer layer on the structural and optical properties of ZnO thin films deposited by E-beam evaporation and sol–gel method, *Applied Surface Science*, 255, 3230-3234, 2008.

[60] Luís D. Carlos, Rute A. S. Ferreira, Verónica de Zea Bermudez, and Sidney J. L. Ribeiro, Lanthanide-Containing Light-Emitting Organic–Inorganic Hybrids: A Bet on the Future, *Advanced Materials*, 21, 509-534, 2009.

[61] H. Yan, Y. Yang, Z. Fu, B. Yang, J. Zuo, S. Fu, Excitation-power dependence of the near-band-edge photoluminescence of ZnO inverse opals and nanocrystal films, *Journal of Luminescence*, 128, 245-249, 2008.

[62] C. Wang, D. Xu, X. Xiao, Y. Zhang, and D. Zhang, Effects of oxygen pressure on the structure and photoluminescence of ZnO thin films, *Journal of Materials Science*, 42, 9795-9800, 2007.

[63] D. Li, Y. H. Leung, A. B. Djurišiæ, Z. T. Liu, M. H. Xie, S. L. Shi, S. J. Xu, and W. K. Chan, Different origins of visible luminescence in ZnO nanostructures fabricated by the chemical and evaporation methods, *Applied Physics Letters*, 85, 1601-1603, 2004.

[64] Eric Lifshin, *X-ray characterisation of materials,* D-69469 Weinheim (Federal Republic of Germany), 1999.

[65] B. Aleksandra, A. Djuriic, C. H. Wallace, A. L. Vellaisamy, Y. H. Leung, C.Y. Kwong, K. W. Cheah, K. G. Tumkur, K. C. Wai, F. L. Hsian, and S. Charles, Photoluminescence and Electron Paramagnetic Resonance of ZnO Tetrapod Structures, *Advanced Functional Materials,* 14, 856-864, 2004.